Projection-based stabilization of interface Lagrange multipliers in immersogeometric fluid–thin structure interaction analysis, with application to heart valve modeling

David Kamensky[a,*], John A. Evans[b], Ming-Chen Hsu[c], Yuri Bazilevs[a]

[a]*Department of Structural Engineering, University of California, San Diego, 9500 Gilman Drive, Mail Code 0085, La Jolla, CA 92093, USA*
[b]*Department of Aerospace Engineering Sciences, University of Colorado at Boulder, 429 UCB, Boulder, CO 80309, USA*
[c]*Department of Mechanical Engineering, Iowa State University, 2025 Black Engineering, Ames, IA 50011, USA*

Abstract

This paper discusses a method of stabilizing Lagrange multiplier fields used to couple thin immersed shell structures and surrounding fluids. The method retains essential conservation properties by stabilizing only the portion of the constraint orthogonal to a coarse multiplier space. This stabilization can easily be applied within iterative methods or semi-implicit time integrators that avoid directly solving a saddle point problem for the Lagrange multiplier field. Heart valve simulations demonstrate applicability of the proposed method to 3D unsteady simulations. An appendix sketches the relation between the proposed method and a high-order-accurate approach for simpler model problems.

Keywords: Fluid–structure interaction; Immersogeometric analysis; Finite cell method; Isogeometric analysis; Projection-based stabilization; Heart valves

Contents

---

*Corresponding author
Email address:* `dmkamensky@eng.ucsd.edu` (David Kamensky)

1. Introduction

Stable coupling of solutions to partial differential equation (PDE) systems discretized on non-matching meshes is a ubiquitous concern in computational mechanics. To fix ideas, consider fluid–structure interaction (FSI) analysis [1], in which fluid and solid mechanics subproblems interact through the constraints that velocity and stress remain continuous across the fluid–structure interface. The fluid–structure interface traction can be interpreted as a Lagrange multiplier associated with the kinematic constraint on the fluid and structure interface velocities (in a sense made precise by [2, Section 2] and Remark 1 in the sequel).

Methods of computing this traction in discrete approximations of FSI problems must therefore satisfy an inf–sup condition [3] to be stable; this condition essentially states that one should not attempt to enforce constraints on the fluid–structure interface at a greater level of detail than the discretized velocity fields can resolve. It is easy to construct a stable discrete space for the Lagrange multiplier field by making it very coarse relative to the fluid and structure discretizations, but this has the obvious consequence of decreasing the approximation power of the discrete space. Disregarding stability, there are many convenient choices of spaces with sufficient approximation power. These multiplier spaces can be salvaged by using strongly-consistent stabilization, as in the method proposed by Barbosa and Hughes [4]. Stenberg [5] later related to the more popular approach of Nitsche [6], in which the Lagrange multiplier is formally eliminated.

While convenient and high-order-accurate, residual-based stabilized schemes such as Barbosa–Hughes stabilization or Nitsche's method lose an important conservation property. To understand this, suppose that the approximation u^h to the solution u of a PDE on a domain, Ω, is constrained to equal the Dirichlet boundary data g, on the boundary $\partial\Omega$. Then we would like to have

$$\int_{\Gamma_E} \left(u^h - g\right) d\Gamma = 0 \,, \qquad \text{(kinematic conservation)} \tag{1}$$

for $\Gamma_E \subset \partial\Omega$. Using a Bubnov–Galerkin discretization with Lagrange multipliers, we have (1) whenever the indicator function on Γ_E is in the test space for the boundary condition constraint. For stabilized methods, (1) does not, in general, hold for any particular Γ_E. To distinguish from other notions of conservation, we refer to (1) as "kinematic conservation".

Consider what this means, physically, in our application of interest: if we do not have kinematic conservation for the no-penetration constraint between the fluid and structure, then a net quantity of fluid can leak through the fluid–structure interface. We have previously demonstrated the importance of kinematic conservation in our work analyzing heart valves [7–11]. Heart valves exist specifically to block flow in one direction and, without kinematic conservation, computational models may not reproduce this important qualitative behavior.

Our previous work sacrificed the stability of the Lagrange multiplier field to achieve satisfactory kinematic conservation. We grudgingly accepted wildly oscillatory multiplier fields, with the consolation that these spurious oscillations appeared to have little-to-no effect on the fluid velocity or structure displacement solutions. This observation is partially supported by *a priori* analysis of simplified model problems in [11, Section 3], but energetic analysis in [9], carefully-constructed numerical experiments, and common sense all indicate that such oscillations are potentially harmful to overall solution quality. In the present study, we cure these oscillations while retaining kinematic conservation by splitting the kinematic constraint into coarse and fine scale components, then stabilizing only the fine scale component of the Lagrange multiplier. The concept of applying projection-based stabilization to boundary and interface Lagrange multipliers was first investigated by Burman [12], in the context of a scalar elliptic model problem; we investigate such a model problem and compare our approach to that of [12] in Appendix A.

We spell out the details of our projection-based stabilization scheme in Section 2 and demonstrate its effectiveness in Section 3, by applying it to FSI analysis, including a simulation of a bioprosthetic heart valve. Section 4 draws conclusions and discusses potential future work on this subject. Appendix A outlines a connection to residual-based stabilization that provides a route to high-order accuracy (on easy problems) and may be of academic interest to some readers.

2. Projection-based stabilization method

This section describes projection-based stabilization of fluid–structure interface Lagrange multipliers. We focus on the case of thin immersed structures, for which the loss of conservation due to residual-based stabilized methods is exacerbated by cancellation of consistency terms (cf. [7, Section 4.1]). Section 2.1 states the fluid–thin structure interaction problem, Section 2.2 describes the projection-stabilized discretization in space, and Section 2.4 adapts the semi-implicit time integration scheme used in [7–11] to include projection-based stabilization.

2.1. Problem statement

This work is focused on the problem of fluid–thin structure interaction, i.e., the case in which the structure is modeled geometrically as a surface of co-dimension one to the fluid subproblem domain into which it is immersed. The ideas from Appendix A could be adapted to general FSI, but that is beyond the scope of the present study.

2.1.1. Augmented Lagrangian formulation of FSI

We start with the augmented Lagrangian framework for FSI [2], specialized to thin immersed structures. The region occupied by incompressible Newtonian fluid is denoted $\Omega_1 \subset \mathbb{R}^d$, where d is the number of spatial dimensions. The structure's midsurface geometry at time t is modeled by a surface $\Gamma_t \subset \Omega_1$, of dimension $d - 1$. The fields $\mathbf{u}_1$ and p are the fluid's velocity and pressure, while $\mathbf{y}$ is the structure's displacement from some reference configuration, Γ_0. $\mathbf{u}_2 \equiv \dot{\mathbf{y}}$ denotes the velocity of the structure. The fluid–structure kinematic constraint, i.e. $\mathbf{u}_1 = \mathbf{u}_2$ on Γ_t, is enforced by the augmented Lagrangian

$$\int_{\Gamma_t} \boldsymbol{\lambda} \cdot (\mathbf{u}_1 - \mathbf{u}_2) \, d\Gamma + \frac{1}{2} \int_{\Gamma_t} \beta |\mathbf{u}_1 - \mathbf{u}_2|^2 \, d\Gamma \, , \tag{2}$$

in which $\boldsymbol{\lambda}$ is a Lagrange multiplier field and $\beta \geq 0$ is a penalization parameter. The resulting weak problem is: Find $\mathbf{u}_1 \in \mathcal{S}_u$, $p \in \mathcal{S}_p$, $\mathbf{y} \in \mathcal{S}_d$, and $\boldsymbol{\lambda} \in \mathcal{S}_\ell$ such that, for all test functions $\mathbf{w}_1 \in \mathcal{V}_u$, $q \in \mathcal{V}_p$, $\mathbf{w}_2 \in \mathcal{V}_d$, and $\delta\boldsymbol{\lambda} \in \mathcal{V}_\ell$

$$B_1(\{\mathbf{u}_1, p\}, \{\mathbf{w}_1, q\}) - F_1(\{\mathbf{w}_1, q\}) + \int_{\Gamma_t} \mathbf{w}_1 \cdot \boldsymbol{\lambda} \, d\Gamma + \int_{\Gamma_t} \mathbf{w}_1 \cdot \beta(\mathbf{u}_1 - \mathbf{u}_2) \, d\Gamma = 0 \, , \tag{3}$$

$$B_2(\mathbf{y}, \mathbf{w}_2) - F_2(\mathbf{w}_2) - \int_{\Gamma_t} \mathbf{w}_2 \cdot \boldsymbol{\lambda} \, d\Gamma - \int_{\Gamma_t} \mathbf{w}_2 \cdot \beta(\mathbf{u}_1 - \mathbf{u}_2) \, d\Gamma = 0 \, , \tag{4}$$

$$\int_{\Gamma_t} \delta\boldsymbol{\lambda} \cdot (\mathbf{u}_1 - \mathbf{u}_2) \, d\Gamma = 0 \, , \tag{5}$$

where $\mathcal{S}_u$, $\mathcal{S}_p$, $\mathcal{S}_d$, and $\mathcal{S}_\ell$ are trial solution spaces for the fluid velocity, fluid pressure, structural displacement, and Lagrange multiplier fields and $\mathcal{V}_u$, $\mathcal{V}_p$, $\mathcal{V}_d$, and $\mathcal{V}_\ell$ are the corresponding test

4

function spaces. B_1, B_2, F_1, and F_2 are semi-linear forms and linear functionals corresponding to the (weak) fluid and structural dynamics problems.

Remark 1. One can easily see from (4) how $\boldsymbol{\lambda}$ acts as a traction on the structure.

2.1.2. Fluid subproblem

As mentioned above, the fluid is modeled as incompressible and Newtonian:

$$B_1(\{\mathbf{u}, p\}, \{\mathbf{w}, q\}) = \int_{\Omega_1} \mathbf{w} \cdot \rho_1 \left(\left. \frac{\partial \mathbf{u}}{\partial t} \right|_{\mathbf{x}} + \mathbf{u} \cdot \boldsymbol{\nabla} \mathbf{u} \right) d\Omega + \int_{\Omega_1} \boldsymbol{\varepsilon}(\mathbf{w}) : \boldsymbol{\sigma}_1 \, d\Omega$$

$$+ \int_{\Omega_1} q \boldsymbol{\nabla} \cdot \mathbf{u} \, d\Omega + \gamma \int_{\Gamma_{1\mathbf{h}}} \mathbf{w} \cdot \rho_1 \langle -\mathbf{u} \cdot \mathbf{n}_1 \rangle \mathbf{u} \, d\Gamma , \tag{6}$$

$$F_1(\{\mathbf{w}, q\}) = \int_{\Omega_1} \mathbf{w} \cdot \rho_1 \mathbf{f}_1 \, d\Omega + \int_{\Gamma_{1\mathbf{h}}} \mathbf{w} \cdot \mathbf{h}_1 \, d\Gamma , \tag{7}$$

where ρ_1 is the mass density of the fluid, $\boldsymbol{\varepsilon}$ is the symmetric gradient, $\boldsymbol{\sigma}_1 = -p\mathbf{I} + 2\mu\boldsymbol{\varepsilon}(\mathbf{u})$ (where μ is the fluid's dynamic viscosity), $\mathbf{f}_1$ is the prescribed body force in the fluid subproblem, and $\mathbf{h}_1$ is the prescribed traction on $\Gamma_{1\mathbf{h}} \subset \partial\Omega_1$. $\partial(\cdot)/\partial t|_{\mathbf{x}}$ indicates time differentiation holding $\mathbf{x}$ in Ω_1 fixed. The last term of (6) is not typically considered part of the weak Navier–Stokes problem, but it enhances stability in cases where flow enters through the Neumann boundary $\Gamma_{1\mathbf{h}}$ [13]; $\langle \cdot \rangle$ are Macaulay brackets, $\mathbf{n}_1$ is the outward-facing normal to Ω_1, and $\gamma > 0$ controls the strength of the stabilization.

2.1.3. Thin structure subproblem

Assuming Kirchhoff–Love thin shell kinematic hypotheses (cf. [14–16]), we define the structure subproblem by

$$B_2(\mathbf{y}, \mathbf{w}) = \int_{\Gamma_t} \mathbf{w} \cdot \rho_2 h_{\text{th}} \left. \frac{\partial^2 \mathbf{y}}{\partial t} \right|_{\mathbf{X}} d\Gamma + \int_{\Gamma_0} \int_{-h_{\text{th}}/2}^{h_{\text{th}}/2} D_{\mathbf{w}} \mathbf{E} : \mathbf{S} \, d\xi^3 d\Gamma \tag{8}$$

and

$$F_2(\mathbf{w}) = \int_{\Gamma_t} \mathbf{w} \cdot \rho_2 h_{\text{th}} \mathbf{f}_2 \, d\Gamma + \int_{\Gamma_t} \mathbf{w} \cdot \mathbf{h}^{\text{net}} \, d\Gamma , \tag{9}$$

where ρ_2 is the structure's mass density, $\mathbf{f}_2$ is a prescribed body force, h_{th} is the thickness of the shell, ξ^3 is a through-thickness coordinate, and we refer the elasticity term to a reference configuration (cf. [1, (1.80)]). The tensor $\mathbf{E}$ is the Green–Lagrange strain corresponding to the displacement $\mathbf{y}$, $D_{\mathbf{w}} \mathbf{E}$ is its functional derivative in the direction of $\mathbf{w}$, and $\mathbf{S}$ is the second Piola–Kirchhoff stress tensor. The last term of F_2 sums the prescribed tractions on the two sides of Γ_t: $\mathbf{h}^{\text{net}} = \mathbf{h}(\xi^3 = -h_{\text{th}}/2) + \mathbf{h}(\xi^3 = +h_{\text{th}}/2)$. $\partial(\cdot)/\partial t|_{\mathbf{X}}$ indicates time differentiation holding $\mathbf{X} \in \Gamma_0$ fixed. The strain $\mathbf{E}$ is simplified to depend only on the shell structure's midsurface displacement,

5

y, to reduce the dimension of the solid mechanics problem. Details of the formulation used in this work are given in [11, Section 2.1.3]. For simplicity, we assume an incompressible neo-Hookean constitutive model, with shear modulus μ_s.

2.2. Stabilized spatial discretization

The fluid and structure subproblems are discretized in space as described in [11]. The principal novelty of the present work is a modification to how the fluid–structure coupling is discretized. Following the general reasoning of [11, Section 2.5.1], we eliminate the tangential component of the kinematic constraint and perturb the normal component to arrive at the problem: Find $\mathbf{u}_1 \in \mathcal{S}_u$, $p \in \mathcal{S}_p$, $\mathbf{y} \in \mathcal{S}_d$, and $\lambda \in \mathcal{S}_\ell$ such that, for all test functions $\mathbf{w}_1 \in \mathcal{V}_u$, $q \in \mathcal{V}_p$, $\mathbf{w}_2 \in \mathcal{V}_d$, and $\delta\lambda \in \mathcal{V}_\ell$

$$
\begin{aligned}
&B_1(\{\mathbf{w}_1, q\}, \{\mathbf{u}_1, p\}) - F_1(\{\mathbf{w}_1, q\}) + B_2(\mathbf{w}_2, \mathbf{y}) - F_2(\mathbf{w}_2) \\
&+ \int_{\Gamma_t} (\mathbf{w}_1 - \mathbf{w}_2) \cdot \lambda \mathbf{n}_2 \, d\Gamma \\
&+ \int_{\Gamma_t} \tau_{\mathrm{NOR}}^B (\mathbf{w}_1 - \mathbf{w}_2)_n (\mathbf{u}_1 - \mathbf{u}_2)_n \, d\Gamma \\
&+ \int_{\Gamma_t} \tau_{\mathrm{TAN}}^B (\mathbf{w}_1 - \mathbf{w}_2)_\Gamma \cdot (\mathbf{u}_1 - \mathbf{u}_2)_\Gamma \, d\Gamma \\
&+ \int_{\Gamma_t} \delta\lambda \cdot \left((\mathbf{u}_1 - \mathbf{u}_2) \cdot \mathbf{n}_2 - \frac{r P^\perp \lambda}{\tau_{\mathrm{NOR}}^B} \right) d\Gamma = 0 \,,
\end{aligned}
\tag{10}
$$

where τ_{TAN}^B is the tangential penalty parameter, τ_{NOR}^B is the normal penalty parameter, $r \geq 0$ controls the strength of the perturbation introduced to stabilize the normal constraint enforcement, and $(\cdot)_n$ and $(\cdot)_\Gamma$ isolate normal and tangential components of $(\cdot)$, i.e. $(\mathbf{v})_n = \mathbf{v} \cdot \mathbf{n}_2$ and $(\mathbf{v})_\Gamma = \mathbf{v} - (\mathbf{v})_n$. The key difference between this problem and [11, (48)–(51)] is the introduction of the projection operator $P^\perp$, highlighted in red.

As suggested by notation, we define $P^\perp$ in terms of another projection operator, P:

$$
P^\perp = I - P \,,
\tag{11}
$$

where I is the identity map. The projection P is an L^2 projection from $\mathcal{V}_\ell$ to $\Lambda^H \subset \mathcal{V}_\ell$: For arbitrary $\lambda \in \mathcal{V}_\ell$,

$$
\left(P\lambda, \delta\lambda^H \right)_{L^2(\Gamma_t)} = \left(\lambda, \delta\lambda^H \right)_{L^2(\Gamma_t)} \qquad \forall \delta\lambda^H \in \Lambda^H \,.
\tag{12}
$$

It is helpful to think of Λ^H as the coarse scales of $\mathcal{V}_\ell$ and $P^\perp \mathcal{V}_\ell$ as the fine scales. The stabilization of the constraint, modulated by r, is applied only to the fine scales of the constraint equation. If we suppose that $\mathcal{V}_\ell$ contains the fluid and structure normal velocity trace spaces on Γ, then we can

directly solve for the multiplier fine scales:

$$P^{\perp}\lambda = \frac{\tau^B_{\text{NOR}}}{r}(\mathbf{u}_1 - \mathbf{u}_2) \cdot \mathbf{n}_2 \tag{13}$$

Taking the penalty augmentations of the Lagrangian into account, fine scale violation of the no-penetration constraint by a velocity difference $(\mathbf{u}_1 - \mathbf{u}_2) \cdot \mathbf{n}_2$ is therefore penalized by the counter-acting force

$$\frac{(1 + r)\tau^B_{\text{NOR}}}{r}\left((\mathbf{u}_1 - \mathbf{u}_2) \cdot \mathbf{n}_2\right)\mathbf{n}_2 . \tag{14}$$

If the effective penalty coefficient $(1 + r)\tau^B_{\text{NOR}}/r$ is considered to be constant, then $r \in (0, \infty)$ is essentially arbitrary, but allowing the lion's share of the penalty to be applied indirectly through $P^{\perp}\lambda$ (i.e. $r \to 0$) may inspire numerical approaches that are better-conditioned than direct penalization (i.e. $r \to \infty \Rightarrow P^{\perp}\lambda \to 0$). An example of such a numerical approach is detailed in Section 2.4 below. The quantity $(1 + r)\tau^B_{\text{NOR}}/r$ is related to the stabilizing penalty of Nitsche's method (as applied to the fine scales of the constraint) by the analysis of Appendix A.

Ideally, the coarse space Λ^H would satisfy the inf–sup condition[1]

$$\inf_{\lambda^H \in \Lambda^H} \sup_{\mathbf{z}^h \in \mathcal{V}^h_u} \frac{{}_{H^{-1/2}(\Gamma)}\left\langle \lambda^H, \mathbf{z}^h \cdot \mathbf{n}_2 \right\rangle_{H^{1/2}(\Gamma)}}{\|\mathbf{z}^h\|_{H^1(\Omega_1)}\|\lambda^H\|_{H^{-1/2}(\Gamma_t)}} \geq C , \tag{15}$$

where $\mathcal{V}^h_u$ is a discrete subspace of $\mathcal{V}_u$ and C is independent of the mesh element size. This condition can be difficult in general to verify, but, given the effectiveness of the two extremes $\Lambda^H = \{0\}$ (as demonstrated by the results of [9, 10]) and $\Lambda^H = \mathcal{V}_\ell$ (i.e. $r = 0$, as applied in [7, 8, 11]), one clearly has, in practice, a great deal of freedom when selecting Λ^H. To narrow down the options, let us itemize several desiderata:

- The space Λ^H should contain the space of constant functions on Γ_t. Ideally, it should contain constants on smaller subsets of Γ_t. This ensures the kinematic conservation property identified in Section 1. Specializing (1) to the FSI problem at hand, a solution of the problem (10) satisfies

$$\int_{\Gamma_E} (\mathbf{u}_1 - \mathbf{u}_2) \cdot \mathbf{n}_2 \, d\Gamma = 0 \tag{16}$$

  (or, in physical terms, no leakage of fluid through Γ_E) whenever the indicator function on $\Gamma_E \subset \Gamma_t$ is in the space Λ^H.

---

[1]One might argue that stability could follow from a similar condition involving structure velocities, but many FSI problems of practical interest entail rigid structures and/or steady limits, in which only the stability characteristics of the fluid and multiplier discrete spaces are relevant.

- The space Λ^H should be coarse and low-order. This improves the likelihood of satisfying (15). Given that, as mentioned above, $\Lambda^H = \{0\}$ produces reasonable results, Λ^H is mainly introduced to satisfy (16). In other words, we are not concerned with the approximation power of Λ^H, only with the conservation properties that it provides. The stabilized fine scales $P^\perp \mathcal{V}_\ell$ can fill in the detailed features of the Lagrange multiplier field. An extension of this concept to high-order-accurate methods (for a simpler model problem) is proposed and analyzed in Appendix A.

In light of the above considerations, the obvious choice is to define Λ^H to be the space of constants on macro-elements covering Γ_t. These macro-elements should have diameters on the order of some length scale H, which is greater than the length scale h associated with the mesh on which $\mathcal{V}_u^h$ is defined. Recalling that the extreme of $\Lambda^H = \{0\}$ works, it is clear that the length scale H need not be refined beyond the point at which satisfactory conservation is obtained. Accuracy can be attained by refining h alone.

2.3. A proposed Λ^H for isogeometric fluid discretizations

In this section, we propose a candidate for Λ^H that is specific to isogeometric fluid discretizations. Suppose that the fluid is discretized on a NURBS or B-spline patch. Then we propose to set Λ^H to the space of constant functions on intersections of Γ_t with groups of 2^d Bézier elements from the background mesh, as shown for $d = 2$ in Figure 1. In some computational frameworks, it may prove convenient to define this space as the trace on Γ_t of a space of d-variate degree-zero B-splines with knot multiplicities alternating between zero and one along each parametric direction. We have not proven that this construction satisfies the condition (15), but we present numerical evidence to support its stability. Our numerical inf–sup test draws on the ideas presented in [17, 18]. In summary, given an inf–sup condition of the form

$$\inf_{p \in Q} \sup_{u \in V} \frac{b(u, p)}{\|u\|_V \|p\|_Q} \geq \beta \, , \tag{17}$$

where b is bilinear, V and Q are finite-dimensional Hilbert spaces, and $\| \cdot \|_V$ and $\| \cdot \|_Q$ are norms induced by inner products $(\cdot, \cdot)_V$ and $(\cdot, \cdot)_Q$, the constant β can be bounded below by the absolute value of the smallest (in magnitude) nonzero eigenvalue satisfying the problem: Find $u \in V$, $p \in Q$, and eigenvalue $\lambda \in \mathbb{R}$ (not to be confused with the interface Lagrange multiplier) such that, for all $v \in V$ and $q \in Q$

$$b(u, q) + b(v, p) = \lambda \left((u, v)_V + (p, q)_Q \right) \, . \tag{18}$$

All eigenvalues are real, due to the symmetry of the problem.

To investigate the stability of our proposed Λ^H, we test (17) with $V \subset H^1(\Omega)$ a scalar uniform
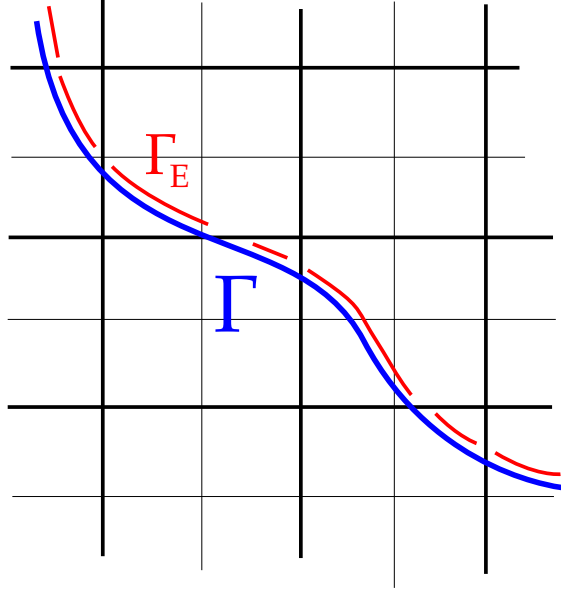
Figure 1: The definition of Lagrange multiplier coarse space macro-elements on a Bézier mesh. Knot lines are black, the immersed surface is blue, and macro-elements are red. Λ^H is the trace on Γ of a space of d-variate degree-zero B-splines in which thick black lines have multiplicity one and thin black lines have multiplicity zero.

B-spline space of maximal continuity on $\Omega = (0, 1)^2 \subset \mathbb{R}^2$, $Q = \Lambda^H \subset H^{-1/2}(\Gamma)$ with $\Gamma = \partial\Omega$, and

$$b(u, \lambda) = {}_{H^{-1/2}(\Gamma)} \langle \lambda, \gamma u \rangle_{H^{1/2}(\Gamma)} \,, \tag{19}$$

where γ is a trace operator mapping from $H^1(\Omega)$ to $H^{1/2}(\Gamma)$. Because (suppressing Riesz maps) $\Lambda^H \subset L^2(\Gamma)$ and $H^{1/2}(\Gamma) \subset L^2(\Gamma)$, we can re-write $b(u, \lambda)$ as simply $(u, \lambda)_{L^2(\Gamma)}$ when restricting to discrete spaces. Direct computation of the $H^{-1/2}(\Gamma)$ inner product (i.e. $(\cdot, \cdot)_Q$ in (18)) is less convenient and, following [5, Section 3], we replace it in the discrete setting with a mesh-dependent inner product,[2]

$$(\lambda, \mu)_{H^{-1/2}(\Gamma)} \quad \rightarrow \quad (\lambda, \mu)_{-1/2,h} \equiv h(\lambda, \mu)_{L^2(\Gamma)} \,, \tag{20}$$

where h is a length scale associated with the element size in a (quasi-uniform) mesh (cf. [5, (3.12)]). For h we simply use the element size of the background mesh defining V. We solve the eigenproblem (18) with meshes of $2^N \times 2^N$ Bézier elements for $N = \{3, 4, 5, 6\}$ and maximally-smooth[3] B-spline spaces (with open knot vectors) of polynomial degree $p = 1, 2, 3, 4$, and 5. Integration over Γ is approximated with a numerical quadrature rule consisting of 100×2^N evenly-

---

[2]This replacement weakens the inf–sup condition, but is sufficient for optimal convergence analysis; see Remark 10 in Appendix A.

[3]Lowering continuity by knot repetition would enrich V, causing the inf–sup constant to either increase or remain the same.

weighted points, evenly spaced along the arc length of Γ. The resulting lower bounds on β are plotted as a function of $\log(h)$ in Figure 2. The fact that these bounds approach constant values as $h \to 0$ indicates that the proposed Λ^H is stable in combination with B-spline spaces of arbitrary degree and continuity. The apparent degree- and continuity-independence of this stability is especially helpful for stable enforcement of boundary conditions on fields discretized using B-splines of mixed degree. Such spaces are used, e.g., to construct isogeometric discrete de Rham complexes [19], to approximate electromagnetic fields [20] and incompressible flows [21, 22].
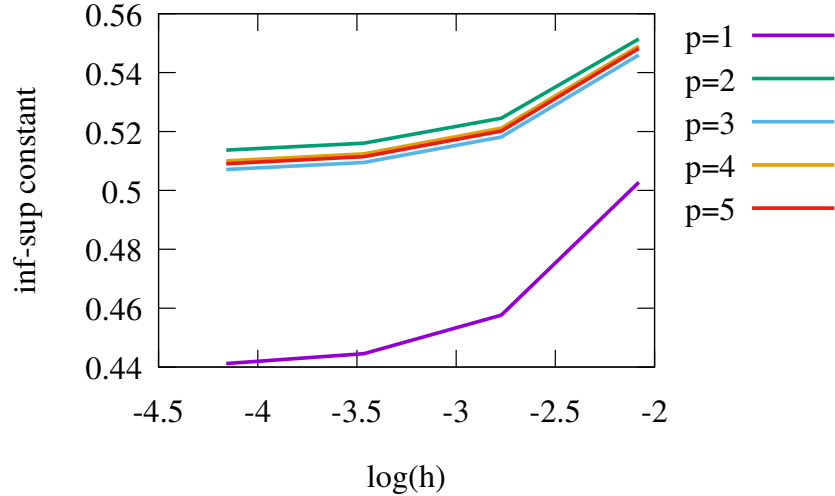

Figure 2: Lower bounds on the inf–sup constant, for different mesh resolutions and polynomial orders, in the case of $\Gamma = \partial\Omega$.

For a general immersed boundary (with $\Gamma \neq \partial\Omega$), the intersections of Γ with blocks of 2^d Bézier elements may have diameters much smaller than h, which is at odds with the assumptions used to arrive at (20). (See [23].) We find that, when using the inner product (20) for discrete inf–sup testing in the immersed setting, it is possible to choose boundary geometries that lead to arbitrarily-small nonzero eigenvalues. However, (20) may not necessarily induce the weakest norm on Λ^H such that the corresponding discrete $H^{+1/2}(\Gamma)$ norm of the error in an $H^1(\Omega)$-optimal interpolant of a regular function still converges at the optimal rate. We nevertheless find that the proposed Λ^H remains practically effective in the immersed setting, as evidenced by the numerical examples in Section 3 and Appendix A.2.

Remark 2. It might be possible to devise a scheme for combining small multiplier macro-elements with adjacent ones, to satisfy the condition (17) uniformly over the space of possible cut element configurations, but we have not explored this possibility in detail.

Remark 3. The apparent degree-independence of the inf–sup constants shown in Figure 2 is a surprising result for B-spline spaces of maximal continuity, since it suggests that kinematic conservation can be stably localized at a length scale of $2h$, even when the supports of basis functions

representing the constrained solution have diameter $(p+1)h$, for $(p+1)$ possibly much larger than 2.

Remark 4. Attempting to devise similar constructions for unstructured fluid discretizations may introduce unacceptable constraints on fluid mesh generation. In such cases, it may prove more effective to define Λ^H in a Lagrangian fashion that follows the structure, as depicted in Figure 3. Stability of such a discretization (in the steady or rigid-structure limits) would be more difficult to establish *a priori*, but preliminary numerical tests (omitted from this work for brevity) suggest that it is a practical option, so long as the elements of Λ^H are coarse enough relative to the fluid discretization. An empirical comparison of Lagrangian and Eulerian constructions of Lagrange multiplier discrete spaces for non-boundary-fitted numerical methods was performed in [24], with the conclusion that the Eulerian (or, in the terminology of [24], "background") construction was much more stable, but the cited study did not consider the possibility of radically-coarsened Lagrangian ("foreground") constructions, which are enabled without loss of accuracy by accounting for (but stabilizing) fine scales of the Lagrange multiplier.
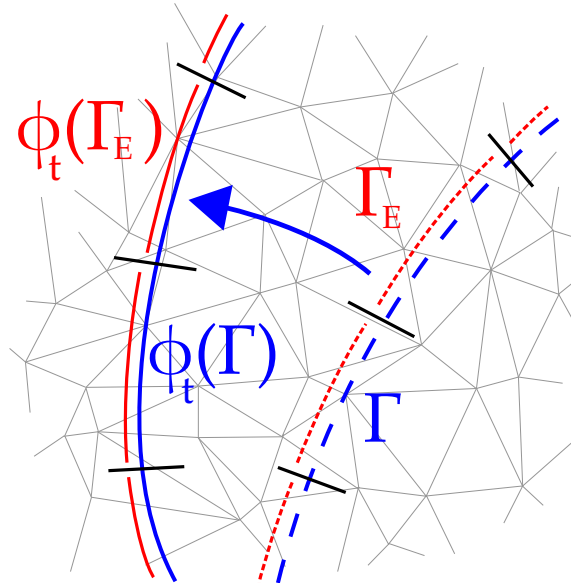

Figure 3: An alternate possibility for defining Lagrange multiplier coarse space macro-elements (cf. Figure 1), using a Lagrangian mesh that deforms according to the fluid–structure interface motion ϕ. (This possibility is not studied in the present paper.)

2.4. Semi-implicit time integration

We now alter the time integration scheme of [11, Section 2.5.2] to accommodate the projector $P^\perp$ in the Lagrange multiplier stabilization. Summarizing briefly, the semi-implicit time integrator described in [11, Section 2.5.2] executes two phases within each time step:

1. Solve (10) while holding λ fixed at its value from the previous time step.

2. Update λ explicitly, using the penalty forces from the solution to step 1.

Only the second phase of updating the Lagrange multiplier field needs to be modified. In [11], the Lagrange multiplier was updated using the formula [11, (70)], namely

$$\lambda^{n+1} = \lambda^n + \tau_{\text{NOR}}^B R^{n+\alpha} , \tag{21}$$

where n is the index of a time step and $R^{n+\alpha}$ is the stabilized "α-level" constraint residual

$$R^{n+\alpha} = \left(\left(\mathbf{u}_1^h\right)^{n+\alpha_f} - \left(\mathbf{u}_2^h\right)^{n+\alpha_f}\right) \cdot \mathbf{n}_2^{n+\alpha_f} - \frac{r\lambda^{n+1}}{\tau_{\text{NOR}}^B} , \tag{22}$$

in which $n + \alpha_f$ indicates an intermediate time level at which the constraint equation is collocated in the integration scheme.[4] The appropriate modification of this update is clear: introduce the projector $P^\perp$ into the last term of (22), i.e.

$$R^{n+\alpha} = \left(\left(\mathbf{u}_1^h\right)^{n+\alpha_f} - \left(\mathbf{u}_2^h\right)^{n+\alpha_f}\right) \cdot \mathbf{n}_2^{n+\alpha_f} - \frac{rP^\perp\lambda^{n+1}}{\tau_{\text{NOR}}^B} . \tag{23}$$

The update (21) then becomes

$$\lambda^{n+1} = \lambda^n + \tau_{\text{NOR}}^B \left\{ \left(\left(\mathbf{u}_1^h\right)^{n+\alpha_f} - \left(\mathbf{u}_2^h\right)^{n+\alpha_f}\right) \cdot \mathbf{n}_2^{n+\alpha_f} - \frac{rP^\perp\lambda^{n+1}}{\tau_{\text{NOR}}^B} \right\} . \tag{24}$$

Using the idempotence and orthogonality of $P^\perp$ and P, we can recast (24) in the form

$$\begin{aligned} \lambda^{n+1} = &P \left(\lambda^n + \tau_{\text{NOR}}^B \left(\left(\mathbf{u}_1^h\right)^{n+\alpha_f} - \left(\mathbf{u}_2^h\right)^{n+\alpha_f}\right) \cdot \mathbf{n}_2^{n+\alpha_f} \right) \\ &+ \left(\frac{1}{1+r}\right) P^\perp \left(\lambda^n + \tau_{\text{NOR}}^B \left(\left(\mathbf{u}_1^h\right)^{n+\alpha_f} - \left(\mathbf{u}_2^h\right)^{n+\alpha_f}\right) \cdot \mathbf{n}_2^{n+\alpha_f} \right) , \end{aligned} \tag{25}$$

which is analogous to [11, (71)]. For $r > 0$, this clearly leads to an exponential decay of the fine scales in the absence of constraint violation, which prevents unchecked growth of spurious modes. This obviously does not satisfy (16) for all t; we only recover (16) in the steady limit, but this is typically sufficient to reap the qualitative benefits of kinematic conservation (as we demonstrate in the sequel).

Remark 5. The update formula (25) does not depend in any way on what Λ^H was in the past. This

---

[4]See [11, Section 2.5.2] for a detailed formulation and [9, Remark 3.1] for a discussion on the use of non-intermediate indexes for λ.

means that (25) naturally accommodates constructions wherein Λ^H (and, consequently, P) change as the structure deforms, such as the proposed Λ^H illustrated in Figure 1.

Remark 6. In addition to reducing the complexity of the discrete problem to be solved at each time step, the semi-implicit integration also permits stability (for transient problems) even when the inf–sup condition (15) is not strictly satisfied by Λ^H. For analysis of a model problem, see [11, Section 3]. It is therefore safer than fully-implicit solution in discretizations for which (15) cannot clearly be established.

Remark 7. If the inf–sup condition (15) holds, then the semi-implicit time integration could be carried out in pseudo-time within each time step, to obtain a fully-implicit solution procedure. This would be equivalent to the classical augmented Lagrangian iteration of Hestenes [25] and Powell [26]. Using such an iteration may be useful for time-independent problems, as it avoids the construction of non-sparse matrices when the coarse scale Lagrange multiplier is discretized on elements very large relative to those used for the constrained solution variable.

Based on dimensional analysis and analogies to Nitsche's method [11, (52)–(53)], we can consider scaling penalty parameters like

$$\tau_{\text{TAN}}^B \sim \mu/h \quad \text{and} \quad \tau_{\text{NOR}}^B \sim \max\left\{\frac{\rho_1 h}{\Delta t}, \frac{\mu}{h}\right\} . \tag{26}$$

In previous work [9, Section 5], we suggested choosing $r \ll 1$ to ensure sufficient conservation. Given coarse-scale kinematic conservation, as provided by the methods of this paper, one has considerably greater freedom in selecting $r \in (0, \infty)$. The steady-state solution (or pseudo-time-converged implicit solution) recovers the penalty interpretation of $P^\perp \lambda$ derived in Section 2.2 (recall (13)–(14)), suggesting that we should select

$$\frac{(1+r)\tau_{\text{NOR}}^B}{r} \sim \max\left\{\frac{\rho_1 h}{\Delta t}, \frac{\mu}{h}\right\} . \tag{27}$$

In that case, r represents a trade-off between (pseudo-)time-accuracy ($r \to \infty$) and ease of solving the implicit step ($r \to 0$, cf. [11, Section 4]) rather than a trade-off between conservation ($r = 0$) and stability ($r = \infty$), as it did in [9], prior to the introduction of a coarse scale space. The scaling expressed through (27) is also supported by the discussion of Appendix A.

3. Numerical examples

We now demonstrate the effects of the proposed projection-based stabilization by applying it in fluid–thin structure interaction simulations.

13

3.1. 2D valve

This section revisits the 2D test problem used to demonstrate convergence with mesh refinement in [11, Section 5]. In brief, the problem (adapted from [27] and studied also in [7, 28–30]) consists of two cantilevered beams attached to the top and bottom of a horizontal channel, driven by a time-periodic velocity boundary condition at the left end of the channel. The Reynolds number is approximately 100. To illustrate the stability of the method proposed in this paper, we rerun the computation on the coarsest mesh, M1, of [11, Section 5.2], using the projection-based stabilization as developed in the prequel. The fluid and structure solutions are essentially the same as those computed in [11, Section 5.3]; readers unfamiliar with the problem are referred to the cited paper for illustrative figures and additional discussion. The similarity of the structure displacement solutions from projection-stabilized and non-stabilized computations (illustrated in Figure 4) indicates that the projection-based stabilization does not interfere with the accuracy of our previous methods, which we demonstrated through refinement studies in [7, 11] and supported with *a priori* error analysis of model problems in [11, Section 3].

We visually illustrate the interface Lagrange multiplier field by plotting its contribution to the traction jump across the thin structure, $\lambda \mathbf{n}_2$. (The total traction jump includes penalty forces in the normal and tangential directions, but these other contributions are omitted for clarity.) Figure 4 compares stabilized Lagrange multiplier fields computed at various times (with $r = \infty$ and Λ^H constructed following Section 2.3) and their non-stabilized counterparts (which can be viewed as taking $\Lambda^H = L^2(\Gamma_t)$, so that $P^\perp = 0$ and the value of r becomes irrelevant). The same values of τ^B_{NOR} and τ^B_{TAN} (from [11, Section 5.2]) are used in both computations. The results in Figure 4 show that the non-stabilized computations, while providing accurate fluid and structure solutions (with beam tip displacements differing from their stabilized counterparts by much less than the size of the fluid elements in the background mesh), produce multiplier fields that appear to diverge as $t \to \infty$ and are therefore not expected to have very-long-time accuracy. The stabilized computations, on the other hand, have bounded multiplier fields that do not exhibit growing oscillations.

To demonstrate the conservation properties of the proposed method, we fill the gap between the leaflets of the 2D valve, so that a single beam extends across the entire channel, blocking it off. We then apply a pressure difference of 10^4 between the ends of the channel. Material and discretization parameters are the same as those used for the previous computation. The equilibrium configuration approached as $t \to \infty$ is shown in Figure 5: the initially-straight beam, cantilevered at both ends, deflects moderately to balance the external pressure difference with internal elastic forces. The volumetric flow rate history is shown in Figure 6. The fact that the flow rate goes to zero as $t \to \infty$ indicates that the kinematic conservation property is satisfied. The high precision with which the correct zero flow rate is recovered in the steady limit indicates that the approximate surface quadrature on Γ_t (discussed in [11, Section 2.4]) is more than sufficient. The multiplier
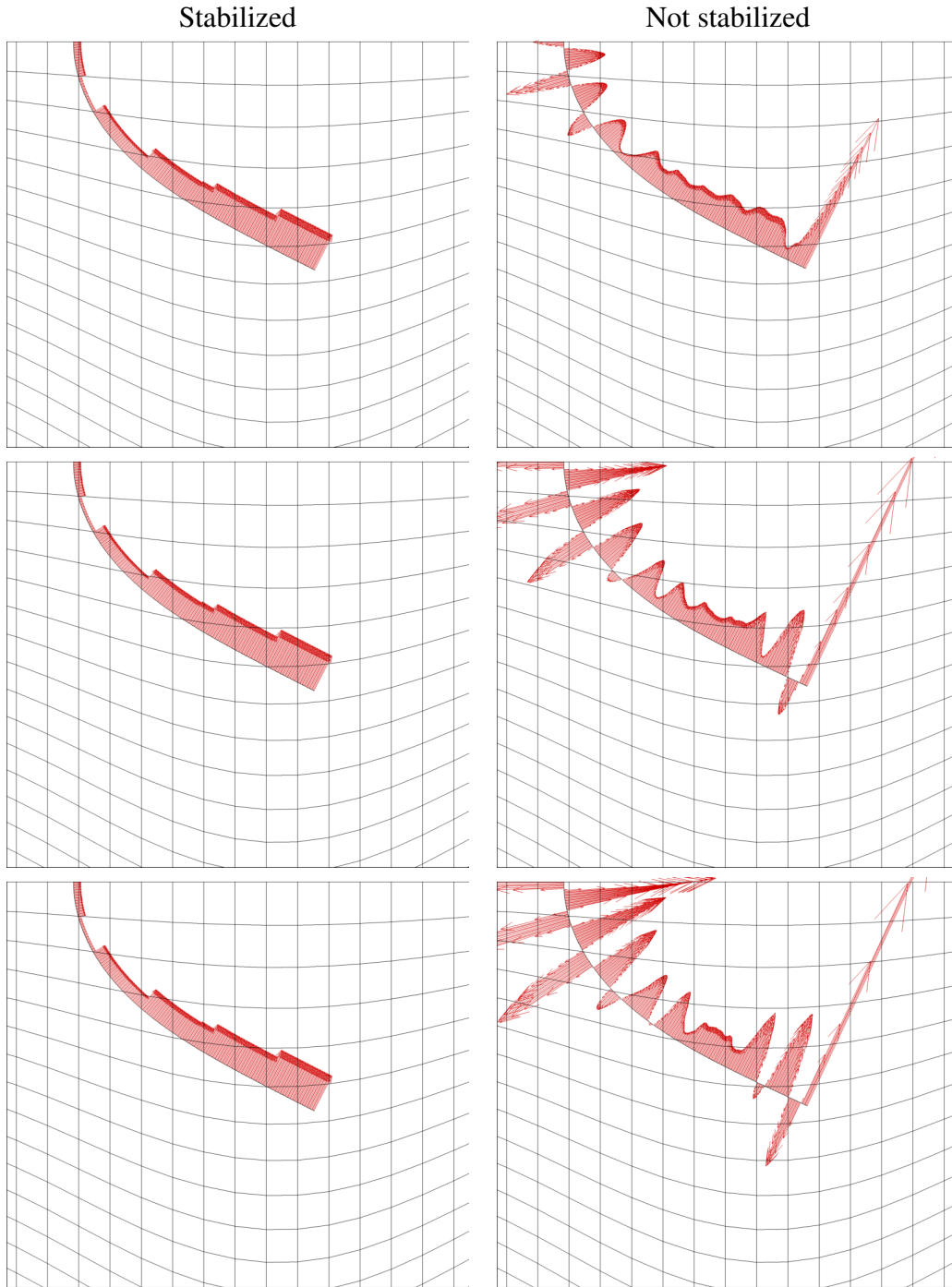
14

Figure 4: Left: the coarse scale Lagrange multiplier's corresponding traction jump at times 0.6 (top), 2.6, and 4.6 (bottom). These snapshots are all taken at the same phase with respect to the time-periodic prescribed data, which has a period of 1. Right: the non-stabilized Lagrange multiplier at the same times, for comparison.

field is shown to be stable in Figure 7, with no oscillations, or even perceptible differences between adjacent macroelements, despite the relatively crude representation of the pressure jump across the beam on a coarse unfitted mesh (as shown in Figure 5).
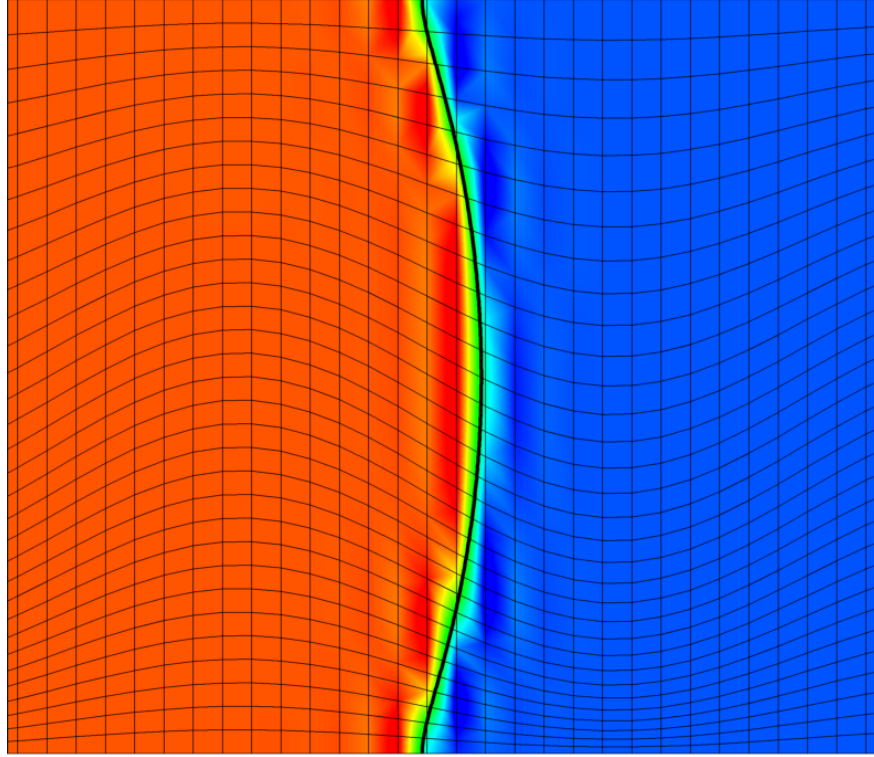
Figure 5: The deformed barrier at $t = 7$ and the fluid pressure field, plotted on a scale from $\leq$-1000 (blue) to $\geq$11000 (red).
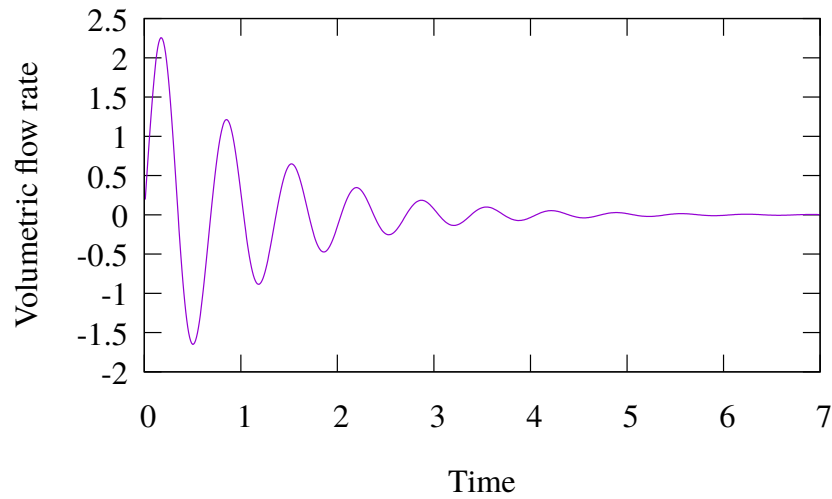

Figure 6: The volumetric flow through the blocked channel. The decaying oscillatory transient can be understood via the electronic–hydraulic analogy depicted in [7, Figure 30]. It is a consequence of the compliance (analogous to: capacitance) of the elastic blockage. In this problem, dissipation is due to the relatively large viscosity.

3.2. Application to heart valve FSI

This section illustrates the practical efficacy of the projection-stabilized, semi-implicitly-integrated Lagrange multiplier method developed in this paper, by applying it to a simulation of
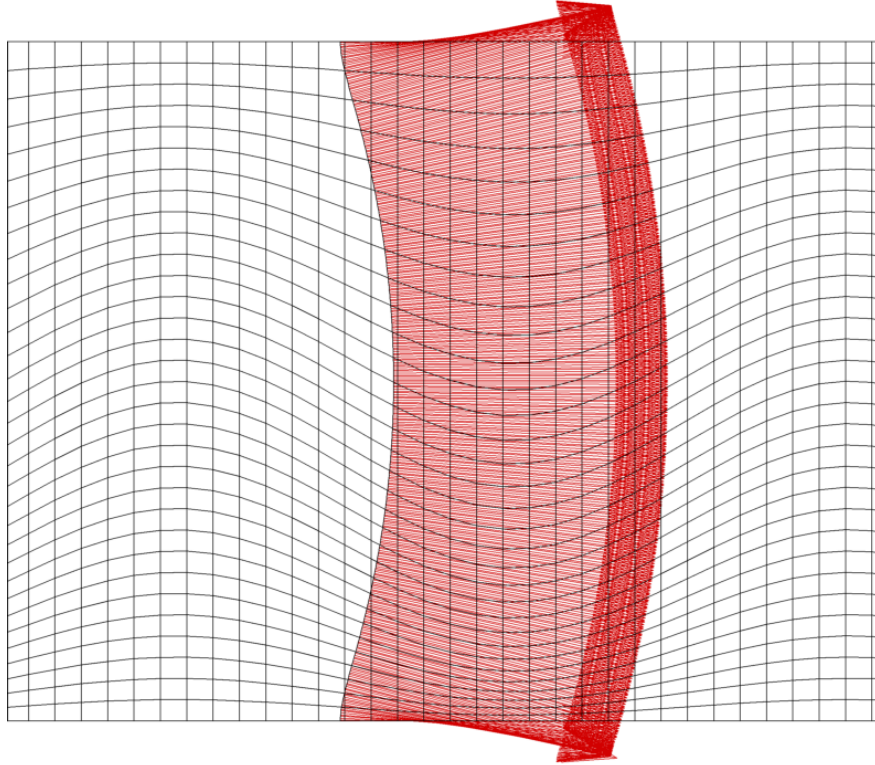
Figure 7: The traction jump corresponding to the Lagrange multiplier field at $t = 7$.

a heart valve subject to physiological pressure levels. The mathematical problem is the same one used in [11, Section 6]. Briefly, a bioprosthetic heart valve (BHV: a type of prosthetic valve used to replace diseased aortic valves) is subjected to an accelerated pressure pulse.[5] The discretization is similar to that used in [11, Section 6], with the following differences:

- The fluid mesh is deliberately coarsened to $30 \times 30 \times 32$ elements, to exacerbate any potential instabilities resulting from an overly-rich Lagrange multiplier space. As we found in [9], coarser fluid meshes are more prone to multiplier oscillations and are therefore more useful for evaluating performance of stabilization approaches. To be clear, we do not advocate using such a coarse fluid mesh if accurate results are desired. For more refined computations using these methods and insight into the relative magnitudes of errors due to modeling and discretization, see [11, Section 7].

- The Lagrange multiplier is discretized in time using the semi-implicit integration method described in Section 2.4 of the current paper, with $r = \infty$. This amounts to applying the penalty method alone to enforce fine scales of the kinematic constraint.

---

[5]Accelerated pulse rates are typically used in industrial testing devices for heart valve prostheses [31].

17

- The cylindrical fluid domain is narrowed to a radius of $R = 1.16$ cm, to reduce gaps in the geometrical model and thus better demonstrate the conservation properties of the numerical approach.

Since the fluid discretization is isogeometric, we employ the coarse multiplier space Λ^H identified in Section 2.3. To demonstrate the effect of stabilization, we compare with a non-stabilized computation (i.e. a computation with $\Lambda^H = L^2(\Gamma_t)$). Differences in the fluid and structure solutions from the two computations are slight, especially relative to the enormous spatial discretization error inherent in using such a coarse fluid mesh to represent a complex flow field. Some snapshots of the fluid and structure solutions are compared in Figure 8. Much larger differences are evident in the multiplier solution: enormous oscillations develop in the non-stabilized multiplier field, as shown in Figure 9. As explained in [9, Section 3.2], these multiplier oscillations can be viewed as storing energy which, under certain circumstances, could be converted back into kinetic and elastic potential energy in the physical subproblems. Allowing multiplier oscillations to grow unchecked may therefore deteriorate very-long-time solution accuracy. Even if it is not always essential for obtaining useful results, it is at least desirable, easily-implemented, and no more computationally expensive to control these oscillations with projection-based stabilization. The conservation properties of the method can be seen by examining the volumetric flow rate through the valve. Figure 10 compares flow rates through the valves in stabilized and non-stabilized computations, demonstrating that the stabilization does not affect the structure's crucial ability to block flow.

4. Conclusions and future work

The methods developed in our previous work forced us to choose between stability (i.e. $r > 0$) and kinematic conservation (i.e. $r \ll 1$ or $r = 0$) when simulating FSI with thin immersed structures. This paper introduces a simple modification, namely projecting the stabilization onto fine scales of the constraint, that allows us to achieve both stability and conservation. We show that, when the multiplier field is approximated using semi-implicit time integration, the projection introduces no additional computational cost and is effective in the challenging setting of heart valve FSI. Appendix A discusses connections between this projection-based stabilization and residual-based stabilization approaches. This connection may indicate a way to generalize the approach to thick structure FSI, but we have not yet fully investigated that possibility.
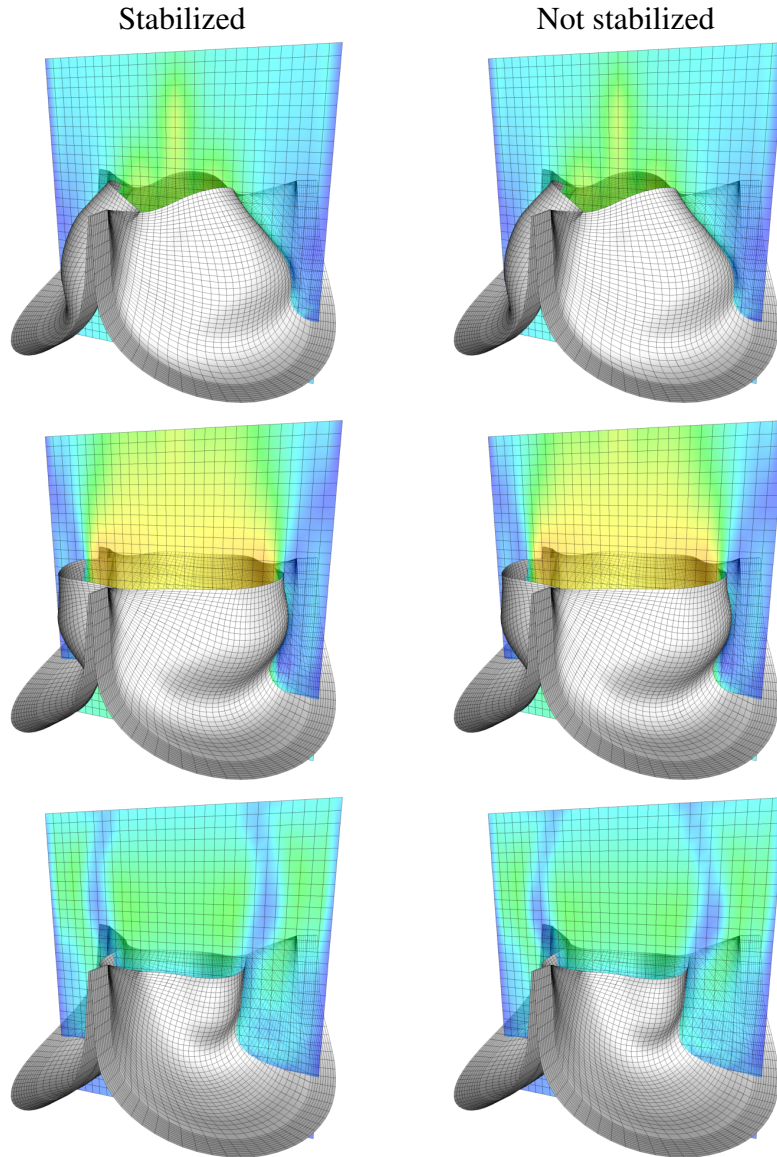
Acknowledgments

Figure 8: **Left:** The structure deformation and a slice of fluid velocity magnitude at times $t = 0.0145$ s (top), $t = 0.0235$ s, and $t = 0.077$ s (bottom) with projection-based stabilization. **Right:** The solution at the same time points, from a different computation without stabilization. **Interpretation:** Colors range from 0 (blue) to ≥ 200 cm/s (red). Stabilized and non-stabilized fluid–structure solutions are nearly identical, at least within short (but still practically-relevant) time scales.
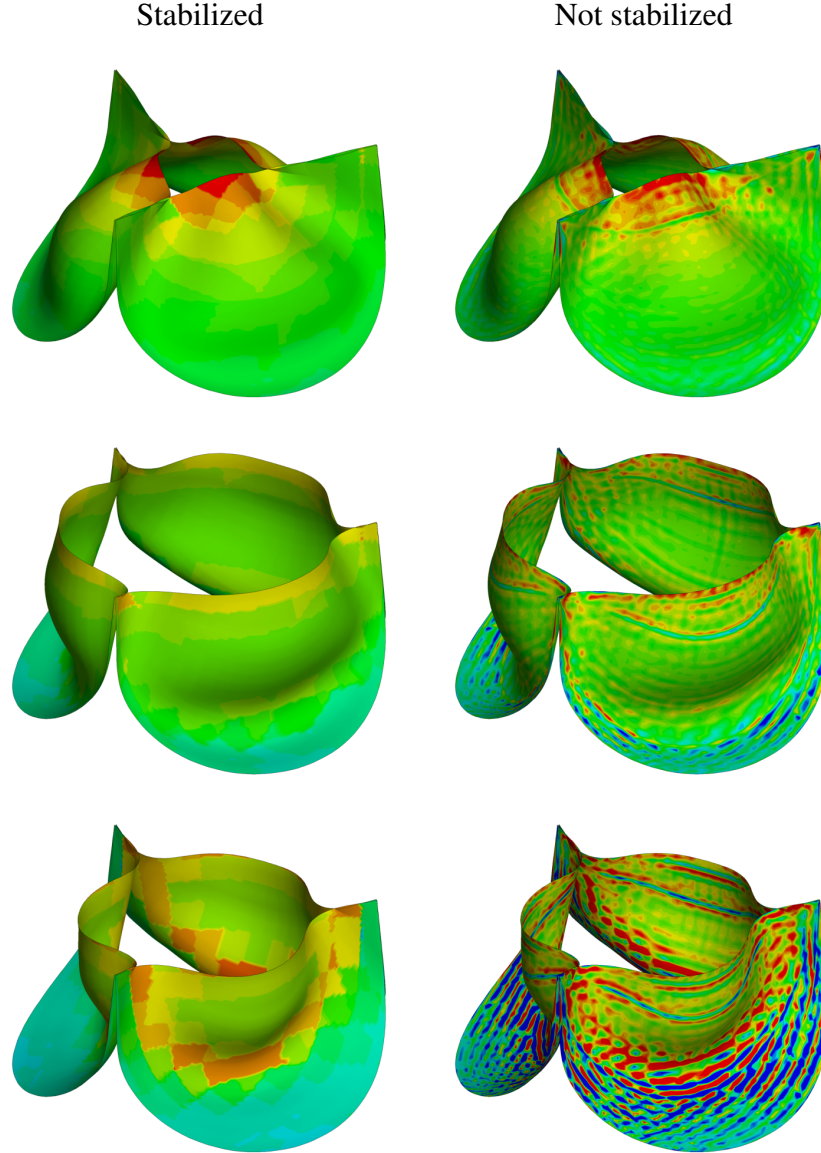
Figure 9: **Left:** The Lagrange multiplier at times $t = 0.0115$ s (top), $t = 0.021$ s, and $t = 0.038$ s (bottom) with projection-based stabilization. **Right:** The Lagrange multiplier at the same time points, from a different computation without stabilization. **Interpretation:** Colors represent the value of the scalar multiplier field λ, using a scale from $\leq -4 \times 10^4$ Ba (blue) to $\geq 10^4$ Ba (red). Note that the maximum and minimum of the non-stabilized multiplier fall very far outside of this range, which is selected to illustrate the variation of the stabilized multiplier. Recall that λ is represented in computations by samples at quadrature points on Γ, as detailed in [11, Sections 2.4 and 2.5]; these point values are linearly interpolated between adjacent quadrature points, for plotting purposes.

Appendix A. Analysis and numerical experiments using a model problem

The idea of using projection-based stabilization for boundary Lagrange multipliers was investigated previously by Burman [12], but the details of the specific numerical methods proposed in Appendix A.1 and [12] vary substantially. What we discuss in this appendix deviates from the typical approach of projection-based stabilization, in that the stabilization of the fine scales re-
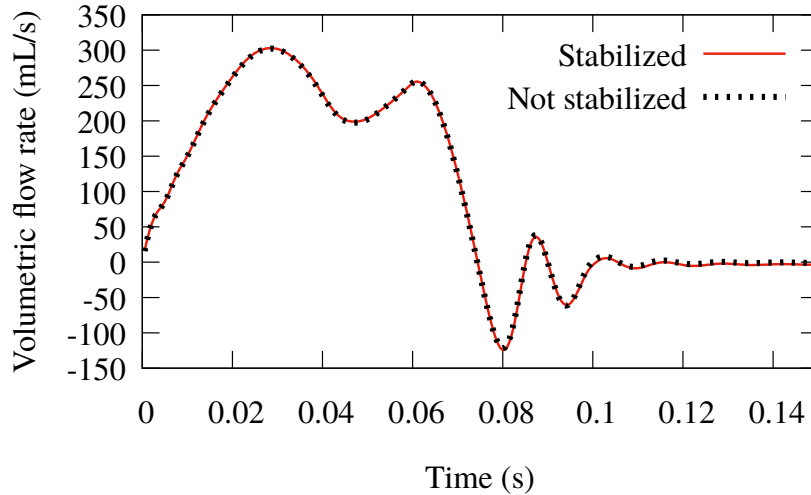
Figure 10: Volumetric flow through the valve with and without stabilization.

mains strongly consistent, while the coarse scales exist solely to enforce conservation properties. The resulting approach does not enjoy many of the typically-cited benefits of projection-based stabilization (as itemized by Burman on [12, page 568]) and, in the thin structure limit, the strong consistency is moot, and the resulting discrete problem could easily be obtained from more traditional projection-based stabilization. However, using consistently-stabilized fine scales eliminates any requirement of approximation power for the coarse Lagrange multiplier space, leaving it with the sole task of enforcing kinematic conservation; this view is more aligned with our interpretation of the fluid–thin structure interaction method presented in the main body of the paper. This thinking bears some resemblance to the work of Chang and Nelson [39] and, later, Evans et al. [40] and Ellis et al. [41], in that it adds low-order Lagrange multipliers on top of an already-convergent numerical method, for the purpose of enforcing conservation or other desirable solution properties. Appendix A.2 applies the numerical method of Appendix A.1 to problems discretized using both conforming and unfitted meshes.

Appendix A.1. Analysis of a model problem

For analysis purposes, we reformulate our numerical method for a second-order linear elliptic model problem. We then extend the arguments of Stenberg [5] to the case of projection-based stabilization. Readers unfamiliar with stabilized Lagrange multiplier methods are encouraged to review Stenberg's analysis.

Appendix A.1.1. Problem setting and notation

We consider an elliptic PDE with Dirichlet boundary conditions:

$$\begin{cases} Lu = -\Delta u + u = f & \text{in } \Omega, \\ u = g & \text{on } \Gamma = \partial\Omega, \end{cases} \tag{A.1}$$

For sufficiently regular u and v,

$$(Lu, v)_{L^2(\Omega)} = a(u, v) = a(v, u) , \tag{A.2}$$

where

$$a(u, v) = (\nabla u, \nabla v)_{L^2(\Omega)} + (u, v)_{L^2(\Omega)} , \tag{A.3}$$

is bounded and coercive in $H^1(\Omega)$.

Remark 8. This problem setting deviates from Stenberg's presentation [5, (2.1)] by adding a reaction term, following Barbosa and Hughes [4, Section 2]. This makes a fully coercive in $H^1(\Omega)$ and simplifies the analysis slightly. Numerical experiments in Appendix A.2 indicate that this reaction term is not strictly necessary.

The weak version of (A.1), using Lagrange multipliers to enforce the Dirchlet boundary condition, is: Find $u \in H^1(\Omega)$ and $\lambda \in H^{-1/2}(\Gamma)$ such that, for all $v \in H^1(\Omega)$ and $\mu \in H^{-1/2}(\Gamma)$,

$$B(\{u, \lambda\}, \{v, \mu\}) = (f, v)_{L^2(\Omega)} - {}_{H^{-1/2}(\Gamma)} \langle \mu, g \rangle_{H^{1/2}(\Gamma)} , \tag{A.4}$$

where

$$B(\{u, \lambda\}, \{v, \mu\}) = a(u, v) + {}_{H^{-1/2}(\Gamma)} \langle \lambda, \gamma v \rangle_{H^{1/2}(\Gamma)} - {}_{H^{-1/2}(\Gamma)} \langle \mu, \gamma u \rangle_{H^{1/2}(\Gamma)} . \tag{A.5}$$

This problem is well-posed, and, for the choice of differential operator L stated above,

$$\lambda = -\nabla u \cdot \mathbf{n} , \tag{A.6}$$

where $\mathbf{n}$ is the normal to $\partial\Omega$. For other differential operators, λ may be equal to a different flux. In the immersed setting, where Γ is an internal surface, ∇u would not be defined in the classical sense and (A.6) would instead hold in the sense of distributions. However, for simplicity, we assume in this section that $\Gamma = \partial\Omega$. In continuum mechanics problems, for example, the interface Lagrange multiplier will be the Cauchy traction (cf. [2, Section 2], for a derivation in the context of FSI).

To compute approximate solutions, let V^h be a conforming finite-dimensional subspace of $H^1(\Omega)$, defined on a mesh of finite elements of size $\sim h$, and let Λ^h be a finite-dimensional subspace of $H^{-1/2}(\Gamma)$ consisting of (inner products with) $L^2(\Gamma)$ functions. Assume that Λ^h is discontinuous

between elements of its own discretization. The assumption of discontinuity can be weakened, but it is easy enough to satisfy in practice, so we retain it here for simplicity.

Now define a *coarse* multiplier space, consisting of constants on macroelements of the mesh defining Λ^h. The macroelements have diameters $\sim H$, and the coarse space is denoted Λ^H. Because Λ^h is discontinuous between elements, it is clearly the case that $\Lambda^H \subset \Lambda^h$. The orthogonal complement of Λ^H in Λ^h (with respect to the $L^2(\Gamma)$ projector) is denoted $\Lambda^\perp \subset \Lambda^h$. As in Section 2.2, we denote the $L^2(\Gamma)$ projection from $L^2(\Gamma)$ to Λ^H as P and define $P^\perp = I - P$ (cf. (11) and (12)). This implies the $L^2(\Gamma)$ orthogonality condition

$$(P^\perp\lambda, P\mu)_{L^2(\Gamma)} = 0 \quad \forall \lambda, \mu \in L^2(\Gamma) \,. \tag{A.7}$$

Because Λ^h is assumed to be discontinuous across macroelement boundaries, the conditions (12) and (A.7) also hold when restricted to individual macroelements.

It is crucial to recognize that **the coarse space's approximation power is irrelevant to the convergence of the numerical approach** defined in the sequel. The coarse mesh parameter H need not even be refined toward zero for the numerical method to converge. It merely indicates the length scale at which the numerical method enforces kinematic conservation. In cases for which global kinematic conservation is sufficient, a single macroelement might be chosen to cover the entire boundary. The only restriction in choosing Λ^H is that it must satisfy the inf–sup condition (A.16), although, given the ability to choose H significantly larger than h, without regard to approximation power, the satisfaction of such conditions becomes quite easy. For instance, the classical result that there exists (*sans* construction) some C, such that (A.16) holds uniformly for $H > Ch$ [3], implies that merely refining h faster than H (which need not be refined at all, from an approximation standpoint) will provide uniform inf–sup stability. Choosing $h \ll H$ may result in poor sparsity patterns in matrix representations of the discrete bilinear form, but this is a non-issue for the iterative and semi-implicit solution schemes discussed in Section 2.4.

Following [5], we define mesh-dependent norms of (traces of) functions in the finite element spaces. The mesh dependent counterpart to $\| \cdot \|_{H^{1/2}(\Gamma)}$ is

$$\|\gamma v\|_{1/2,h}^2 = \sum_E h_E^{-1} \|\gamma v\|_{L^2(\Gamma_E)}^2 \,, \tag{A.8}$$

for all $v \in H^1(\Omega)$, where E indexes macroelements $\{\Gamma_E\}$ of the coarse-scale mesh of Γ, and h_E asymptotically bounds, from above and below, the sizes of elements from the mesh defining V^h that intersect Γ_E. (The length scale h_E is not, in general, proportional to the diameter of Γ_E.) With this assumption of quasi-uniformity within macroelements, (A.8) is equivalent (up to constants) to the definition of $\| \cdot \|_{1/2,h}$ given by Stenberg [5, (3.11)]. The analog of the $\| \cdot \|_{H^{-1/2}(\Gamma)}$ norm for finite

23

element functions in $\Lambda^h \subset L^2(\Gamma) \subset H^{-1/2}(\Gamma)$ is

$$\|z\|^2_{-1/2,h} = \sum_E h_E \|z\|^2_{L^2(\Gamma_E)} \, , \tag{A.9}$$

for all $z \in L^2(\Gamma)$. This is, of course, also a norm on the coarse space $\Lambda^H \subset \Lambda^h$. It follows that

$$_{H^{-1/2}(\Gamma)} \langle z, \gamma v \rangle_{H^{1/2}(\Gamma)} \leq \|\gamma v\|_{1/2,h} \|z\|_{-1/2,h} \quad \forall \{v, z\} \in H^1(\Omega) \times L^2(\Gamma) \, . \tag{A.10}$$

Recalling that, when arguments are in $L^2(\Gamma)$, $_{H^{-1/2}(\Gamma)} \langle \cdot, \cdot \rangle_{H^{1/2}(\Gamma)}$ is equivalent to $(\cdot, \cdot)_{L^2(\Gamma)}$, we define, as a reminder,

$$\langle u, v \rangle_A = (u, v)_{L^2(A)} \, , \tag{A.11}$$

for $A \subset \Gamma$ and $u, v \in L^2(\Gamma)$. We then construct a norm on the product space $V^h \times \Lambda^h$:

$$\|u, \lambda\|^2 = \|u\|^2_{H^1(\Omega)} + \|\lambda\|^2_{-1/2,h} \tag{A.12}$$

for all $u \in H^1(\Omega)$ and $\lambda \in L^2(\Gamma)$. Given standard interpolation estimates [5, Lemma 2] and assuming sufficient regularity of u and λ, we can then show optimal convergence if consistency, stability, and boundedness of a discrete formulation are satisfied with respect to the $\|\cdot, \cdot\|$ norm. To show stability of the discrete formulation discussed in the sequel, we need the trace-inverse estimate [5, Lemma 3]:

$$C_I \left\| \nabla v^h \cdot \mathbf{n} \right\|_{-1/2,h} \leq \|v^h\|_{H^1(\Omega)} \, , \tag{A.13}$$

for all $v^h \in V^h$. For a different differential operator L in (A.1), a similar identity would be needed for whatever the relevant boundary flux is.

Appendix A.1.2. Numerical method

The finite-dimensional approximation to (A.4) that we want to solve is: Find $u^h \in V^h$ and $\lambda^h \in \Lambda^h$ such that, for all $v^h \in V^h$ and $\mu^h \in \Lambda^h$,

$$B_h(\{u^h, \lambda^h\}, \{v^h, \mu^h\}) = (f, v^h)_{L^2(\Omega)} + {}_{H^{-1/2}(\Gamma)} \left\langle \mu^h, -g \right\rangle_{H^{1/2}(\Gamma)} \, , \tag{A.14}$$

where

$$\begin{aligned} B_h(\{u^h, \lambda^h\}, \{v^h, \mu^h\}) = &B(\{u^h, \lambda^h\}, \{v^h, \mu^h\}) \\ &- \alpha \sum_E h_E \left\langle P^\perp \left(\lambda^h + \nabla u^h \cdot \mathbf{n} \right), P^\perp \left(-\mu^h + \nabla v^h \cdot \mathbf{n} \right) \right\rangle_{\Gamma_E} \, . \end{aligned} \tag{A.15}$$

$\alpha > 0$ is a stabilization parameter. The sum $\sum_E$ indicates summation over macroelements Γ_E indexed by E, containing fine scale elements of size $\sim h_E$.

Remark 9. Because the orthogonality condition (A.7) holds on each macroelement Γ_E, we can safely remove $P^\perp$ from one side of the duality pairing in the stabilization term. This would *not* be true if the sum were instead taken over fine scale elements with a different length scale h_e on each element. The coarse mesh is the finest scale at which we have L^2 orthogonality between Λ^h and Λ^H.

Assuming $\lambda \in L^2(\Gamma)$, the strong consistency of this formulation is clear. For optimal convergence, we need a stability result. We begin by making a stability assumption about the coarse space. Specifically, we assume that it satisfies

$$\inf_{\lambda^H \in \Lambda^H} \sup_{z^h \in V^h} \frac{{}_{H^{-1/2}(\Gamma)}\left\langle \lambda^H, \gamma z^h \right\rangle_{H^{1/2}(\Gamma)}}{\|z^h\|_{H^1(\Omega)}\|\lambda^H\|_{-1/2,h}} \geq C_{\mathrm{Br}} , \tag{A.16}$$

where C_{Br} is independent of h. This implies [42, Section 5]

$$\inf_{(v,\mu)\in V^h\times\Lambda^H} \sup_{(z,\eta)\in V^h\times\Lambda^H} \frac{B_h(\{v,\mu\},\{z,\eta\})}{\vertiii{z,\eta}\vertiii{v,\mu}} \geq C_{\mathrm{Ba}} , \tag{A.17}$$

under the condition that the bilinear form

$$a_\alpha(u,v) = a(u,v) - \alpha \sum_E h_E \left\langle P^\perp \nabla u \cdot \mathbf{n}, P^\perp \nabla v \cdot \mathbf{n} \right\rangle_{\Gamma_E} \tag{A.18}$$

is continuous and coercive in V^h [42, Section 5]. The continuity of a_α is a consequence of the trace-inverse estimate (A.13). The coercivity of a_α follows from the standard condition on the Barbosa–Hughes stabilization parameter:

$$\alpha = \frac{C_I C_A}{2} , \tag{A.19}$$

where C_A is the coercivity constant of a in $H^1(\Omega)$. Defining α as above, recalling the coercivity of a and the trace-inverse inequality (A.13), and noting that the induced $L^2(\Gamma_E)$ norm of the orthogonal projector $P^\perp$ is ≤ 1,

$$a_\alpha(v,v) \geq C_A\|v\|^2_{H^1(\Omega)} - \alpha\,\|\nabla v \cdot \mathbf{n}\|^2_{-1/2,h} \geq \left(C_A - \frac{\alpha}{C_I}\right)\|v\|^2_{H^1(\Omega)} = \frac{C_A}{2} . \tag{A.20}$$

The inf–sup condition we want for optimal convergence replaces the space Λ^H in (A.17) with the

full multiplier space Λ^h:

$$\inf_{(v,\mu)\in V^h\times\Lambda^h} \sup_{(z,\eta)\in V^h\times\Lambda^h} \frac{B_h(\{v,\mu\},\{z,\eta\})}{\|z,\eta\|\|v,\mu\|} \overset{\heartsuit}{\geq} C_{\text{inf–sup}}\,, \tag{A.21}$$

where $\heartsuit$ indicates a desired relation that remains to be established. However, we can use (A.17) to obtain the desired inf–sup condition for the formulation (A.14). First, observe that having (A.17) allows us to limit our testing of (A.21) to the fine scale multiplier discrete space, $\Lambda^\perp$:

$$\inf_{(v,\mu)\in V^h\times\Lambda^h} \sup_{(z,\eta)\in V^h\times\Lambda^h} \frac{B_h(\{v,\mu\},\{z,\eta\})}{\|z,\eta\|\|v,\mu\|}$$

$$= \min\left\{ \inf_{(v,\mu)\in V^h\times\Lambda^H} \sup_{(z,\eta)\in V^h\times\Lambda^h} \frac{B_h(\{v,\mu\},\{z,\eta\})}{\|z,\eta\|\|v,\mu\|} \,,\, \inf_{(v,\mu)\in V^h\times\Lambda^\perp} \sup_{(z,\eta)\in V^h\times\Lambda^h} \frac{B_h(\{v,\mu\},\{z,\eta\})}{\|z,\eta\|\|v,\mu\|} \right\} \tag{A.22}$$

$$\geq \min\left\{ \inf_{(v,\mu)\in V^h\times\Lambda^H} \sup_{(z,\eta)\in V^h\times\Lambda^H} \frac{B_h(\{v,\mu\},\{z,\eta\})}{\|z,\eta\|\|v,\mu\|} \,,\, \inf_{(v,\mu)\in V^h\times\Lambda^\perp} \sup_{(z,\eta)\in V^h\times\Lambda^h} \frac{B_h(\{v,\mu\},\{z,\eta\})}{\|z,\eta\|\|v,\mu\|} \right\} \tag{A.23}$$

$$\geq \min\left\{ C_{\text{Ba}} \,,\, \inf_{(v,\mu)\in V^h\times\Lambda^\perp} \sup_{(z,\eta)\in V^h\times\Lambda^\perp} \frac{B_h(\{v,\mu\},\{z,\eta\})}{\|z,\eta\|\|v,\mu\|} \right\}\,. \tag{A.24}$$

What we want to complete our argument is then

$$\inf_{(v,\mu)\in V^h\times\Lambda^\perp} \sup_{(z,\eta)\in V^h\times\Lambda^\perp} \frac{B_h(\{v,\mu\},\{z,\eta\})}{\|z,\eta\|\|v,\mu\|} \overset{\heartsuit}{\geq} C_\alpha\,, \tag{A.25}$$

with C_α independent of h. This will secure the desired inequality (A.21), with $C_{\text{inf–sup}} = \min\{C_{\text{Ba}}, C_\alpha\}$. The inequality (A.25) follows easily from standard analysis of Barbosa–Hughes stabilization, using the definition of α given by (A.19) and recalling that, for all $\lambda\in\Lambda^\perp$, $P^\perp\lambda=\lambda$. We can resort to the special case of coercivity of B_h when restricted to the space $V^h\times\Lambda^\perp$. For arbitrary $v\in V^h$ and $\mu\in\Lambda^\perp$,

$$B_h(\{v,\mu\},\{v,\mu\}) = a(v,v) - \alpha\sum_E h_E\left\langle P^\perp\left(\mu+\nabla v\cdot\mathbf{n}\right), P^\perp\left(-\mu+\nabla v\cdot\mathbf{n}\right)\right\rangle_{\Gamma_E} \tag{A.26}$$

$$= a_\alpha(v,v) + \alpha\sum_E h_E\|\mu\|^2_{L^2(\Gamma_E)} \qquad \text{(Recall the definition (A.18) of } a_\alpha.) \tag{A.27}$$

$$\geq \frac{C_A}{2}\|v\|^2_{H^1(\Omega)} + \frac{C_A C_I}{2}\|\mu\|^2_{-1/2,h} \tag{A.28}$$

$$\geq \min\left\{\frac{C_A}{2}, \frac{C_A C_I}{2}\right\}\|v,\mu\|^2\,. \tag{A.29}$$

Therefore, combining (A.24) and (A.29), we obtain our goal of (A.21), with

$$C_{\text{inf–sup}} \geq \min\left\{C_{\text{Ba}}, \frac{C_A}{2}, \frac{C_A C_I}{2}\right\}. \tag{A.30}$$

With an appropriate selection of the stabilization parameter, we therefore have optimal convergence of the numerical method. Unlike the usual Barbosa–Hughes approach, though, we have some degree of local conservation, on the macroelements of the coarse multiplier space.

Remark 10. A minor subtlety is that B_h is not uniformly bounded in the norm $\|\|\cdot\|\|$, so deriving optimal convergence from (A.21) follows a non-standard procedure. The use of inf–sup stability and strong consistency follows in the usual way to give us

$$C_{\text{inf–sup}}\|\|e_u^h, e_\lambda^h\|\| \leq \sup_{v^h, \mu^h} \frac{B_h(\{\eta_u, \eta_\lambda\}, \{v^h, \mu^h\})}{\|\|v^h, \mu^h\|\|}, \tag{A.31}$$

in which the total error is given by $e = \eta + e^h$, where e^h is in the discrete space and η is the optimally-small interpolation error. Boundedness of B_h in $\|\|\cdot\|\|$ would obviously complete the analysis, but is not strictly necessary. The interpolation assumption [4, (H9)] easily implies the weaker-but-sufficient condition

$$\left|B_h(\{\eta_u, \eta_\lambda\}, \{v^h, \mu^h\})\right| \leq (\text{optimal in } h)\|\|v^h, \mu^h\|\| \qquad \forall v^h, \mu^h. \tag{A.32}$$

Appendix A.1.3. Formal elimination of fine scales

Adapting the argument from [5, page 146], we can formally eliminate the fine scale component of the Lagrange multipliers by first noting, from (A.14), that, on each macroelement Γ_E and for each test function $\mu^h \in \Lambda^h$,

$$\left\langle P^\perp \lambda^h, \mu^h \right\rangle_{\Gamma_E} = \left\langle -P^\perp\left(\nabla u^h \cdot \mathbf{n}\right) + \frac{1}{\alpha h_E} P^\perp\left(u^h - g\right), \mu^h \right\rangle_{\Gamma_E}. \tag{A.33}$$

Then, if we set $\Lambda^h = L^2(\Gamma)$, set $\mu^h = \mu^H \in \Lambda^H$ in (A.14), insert the right-hand side of (A.33) in lieu of $P^\perp \lambda^h$, and denote $P\lambda^h$ as $\lambda^H \in \Lambda^H$, we can obtain the following problem, which is devoid of any explicit representation of multiplier fine scales: Find $u^h \in V^h$ and $\lambda^H \in \Lambda^H$ such that, for all $v^h \in V^h$ and $\mu^H \in \Lambda^H$,

$$a(u^h, v^h) + {}_{H^{-1/2}(\Gamma)}\left\langle \lambda^H, v^h \right\rangle_{H^{1/2}(\Gamma)} - {}_{H^{-1/2}(\Gamma)}\left\langle \mu^H, u^h - g \right\rangle_{H^{1/2}(\Gamma)}$$
$$- {}_{H^{-1/2}(\Gamma)}\left\langle P^\perp\left(\nabla u^h \cdot \mathbf{n}\right), P^\perp v^h \right\rangle_{H^{1/2}(\Gamma)} - {}_{H^{-1/2}(\Gamma)}\left\langle P^\perp\left(\nabla v^h \cdot \mathbf{n}\right), P^\perp(u^h - g) \right\rangle_{H^{1/2}(\Gamma)}$$
$$+ \sum_E (\alpha h_E)^{-1}\langle P^\perp(u^h - g), P^\perp v^h\rangle_{\Gamma_E} = (f, v^h)_{L^2(\Omega)}. \tag{A.34}$$

27

The above is essentially using coarse multipliers to enforce conservation on macroelements and Nitsche's method to obtain fine scale accuracy in the constraint.

Appendix A.1.4. Formal elimination of the projection

Some formal manipulations simplify the implementation of (A.34). First, we can use orthogonality to eliminate redundant projections:

$$
\begin{aligned}
a(u^h, v^h) + {}_{H^{-1/2}(\Gamma)}\left\langle \lambda^H, v^h \right\rangle_{H^{1/2}(\Gamma)} &- {}_{H^{-1/2}(\Gamma)}\left\langle \mu^H, u^h - g \right\rangle_{H^{1/2}(\Gamma)} \\
- {}_{H^{-1/2}(\Gamma)}\left\langle P^{\perp}\left(\nabla u^h \cdot \mathbf{n}\right), v^h \right\rangle_{H^{1/2}(\Gamma)} &- {}_{H^{-1/2}(\Gamma)}\left\langle \nabla v^h \cdot \mathbf{n}, u^h - g \right\rangle_{H^{1/2}(\Gamma)} \\
+ \sum_E (\alpha h_E)^{-1}\langle u^h - g, v^h \rangle_{\Gamma_E} &= (f, v^h)_{L^2(\Omega)} \,.
\end{aligned}
\tag{A.35}
$$

Then we can define a new variable

$$
\lambda_0^H = \left(\lambda^H + P\left(\nabla u^h \cdot \mathbf{n}\right)\right) \in \Lambda^H
\tag{A.36}
$$

and rephrase the problem in terms of λ_0^H: Find $u^h \in V^h$ and $\lambda_0^H \in \Lambda^H$ such that, for all $v^h \in V^h$ and $\mu^H \in \Lambda^H$,

$$
\begin{aligned}
a(u^h, v^h) + {}_{H^{-1/2}(\Gamma)}\left\langle \lambda_0^H, v^h \right\rangle_{H^{1/2}(\Gamma)} &- {}_{H^{-1/2}(\Gamma)}\left\langle \mu^H, u^h - g \right\rangle_{H^{1/2}(\Gamma)} \\
- {}_{H^{-1/2}(\Gamma)}\left\langle \nabla u^h \cdot \mathbf{n}, v^h \right\rangle_{H^{1/2}(\Gamma)} &- {}_{H^{-1/2}(\Gamma)}\left\langle \nabla v^h \cdot \mathbf{n}, u^h - g \right\rangle_{H^{1/2}(\Gamma)} \\
+ \sum_E (\alpha h_E)^{-1}\langle u^h - g, v^h \rangle_{\Gamma_E} &= (f, v^h)_{L^2(\Omega)} \,.
\end{aligned}
\tag{A.37}
$$

λ_0^H should obviously converge to zero under refinement. However, its presence ensures conservation on macroelements. Computationally, this is just Nitsche's method for all scales of the constraint, with an extra layer of coarse scale Lagrange multipliers ensuring conservation.

The original λ^H from the problem (A.37) can be extracted by post-processing via (A.36). However, the typical quantity of interest one would want to calculate would be the conservative flux (cf. [43])

$$
- \lambda^h = -(\lambda^H + P^{\perp}\lambda^h) = -\lambda_0^H + \nabla u^h \cdot \mathbf{n} - (\alpha h_E)^{-1}(u^h - g)\,,
\tag{A.38}
$$

so the entire computation and typical post-processing tasks do not require the projector P.

Appendix A.2. Numerical examples

This section demonstrates the applicability of the preceding analysis to boundary-fitted and immersed discretizations some elliptic model problems.

Appendix A.2.1. Poisson problem on a fitted mesh

This section tests convergence to a manufactured solution of the Poisson problem on a square domain. In particular, we approximate solutions to the problem:[6] Find u such that

$$\begin{cases} -\Delta u = f & \text{on } \Omega \\ \quad u = g & \text{on } \partial\Omega \,, \end{cases} \tag{A.39}$$

with $\Omega = (0,1) \times S^1$ (i.e., a unit square with periodicity in the x_2 direction). We manufacture a smooth exact solution

$$u_{\text{exact}}(\mathbf{x}) = \frac{1}{2}\left(1 - \cos(2\pi x_2)\right)\sin\left(\frac{\pi}{2}\left(x_1 - \frac{1}{2}\right)\right), \tag{A.40}$$

by setting $f = -\Delta u_{\text{exact}}$ and $g = u_{\text{exact}}|_{\partial\Omega}$ and apply the discretization given in Appendix A.1.4. V^h is a B-spline space of polynomial degree 4 and maximal continuity, with $2^N \times 2^N$ Bézier elements, for $N = \{3,\ldots,7\}$. Λ^H is the space propsed in Section 2.3, which, although presented in the context of immersed boundaries, can clearly also be used when Γ happens to coincide with the boundary of a conforming mesh. The mesh size h_E is set to the width of a single Bézier element and the constant α is set to one. The convergence of approximate solutions in $L^2(\Omega)$ and $H^1(\Omega)$ is shown in Figure A.11, exhibiting optimal rates, as expected. To show the effect of the conservation properties of
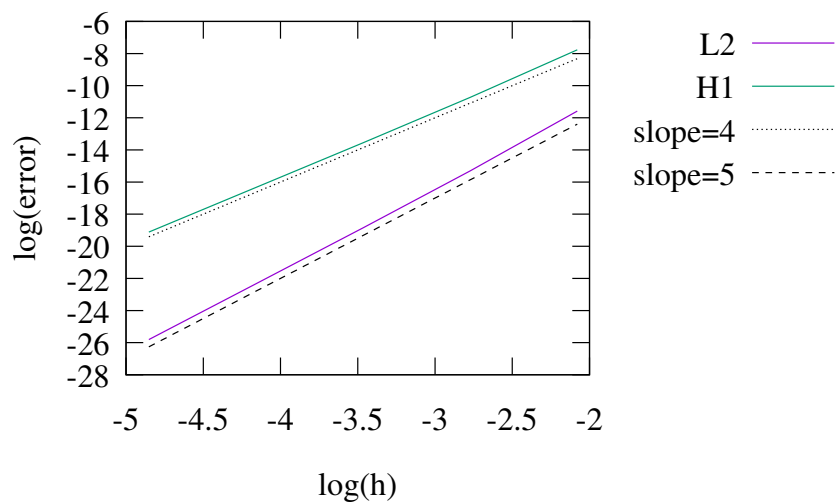

Figure A.11: Convergence of $L^2(\Omega)$ and $H^1(\Omega)$ errors using a fitted mesh, showing optimal rates for $p = 4$.

---

[6]The differential operator of problem (A.39) differs from that analyzed in Appendix A.1, but adapting the numerical methods developed for (A.1) to problem (A.39) is trivially straightforward. The efficacy of these numerical methods on problem (A.39) indicates the non-necessity of the reaction term added to (A.1) for convenience.

the numerical method, we compute the integral

$$E = \int_{0.25}^{0.375} \left(\gamma u^h (0, x_2) - g(x_2) \right) \, dx_2 \tag{A.41}$$

for all N. For $N \geq 4$, the integration domain $(0.25, 0.375)$ is a union of coarse scale multiplier elements. Therefore, for $N \geq 4$, we expect E to hover within machine precision of zero whereas, for $N < 4$ the integration domain covers only part of a coarse scale multiplier element and, we expect E to be influenced by discretization error (which is typically much larger than floating-point round-off error). The results of this experiment are show in Table A.1

Table A.1: We expect E to be machine zero for $N \geq 4$, due to the conservation properties of the numerical method.

N	E
3	1.92×10^{-7}
4	4.45×10^{-17}
5	8.33×10^{-18}
6	-1.19×10^{-17}
7	-9.83×10^{-18}

Appendix A.2.2. Poisson problem on an unfitted mesh

We now consider an unfitted discretization of the Poisson problem, in which some of the tacit assumptions justifying the selection of discrete $H^{\pm 1/2}(\Gamma)$ norms in Appendix A.1 may not hold. The test problem is the same as that described in Appendix A.2.1, aside from the definition of Ω, which is modified to be

$$\Omega = (0, 1)^2 \setminus \left\{ \mathbf{x} \in \mathbb{R}^2 \,\middle|\, \|\mathbf{x}\|_{\ell^2} \leq 0.25 \right\}, \tag{A.42}$$

again with periodicity in the x_2-direction. A representative numerical solution is shown in Figure A.12. We again discretize the field u using B-spline spaces defined on the rectangle $(0, 1)^2$ (now restricted to $\Omega \subsetneq (0, 1)^2$). To integrate the variational formulation of Appendix A.1.4 over a region that does not conform to element boundaries, we use a numerical approach called the finite cell method, reviewed in [44]. The finite cell method makes use of a procedure termed "adaptive quadrature" to resolve integrals over elements cut by the domain boundary: quadrature cells intersecting an immersed boundary are recursively subdivided until a sufficient degree of accuracy is obtained. Implementation details are as specified in [7, Section 3.2]. In particular, we follow the notation of [7, Section 3.2] and use the symbol l to denote the level of adaptive quadrature, i.e., the maximum depth of recursion used to generate adaptive quadrature rules in elements intersected by the immersed boundary. To test convergence, we discretize u in this problem with $2^N \times 2^N$-element B-spline spaces of maximal continuity and polynomial degree $p = 2$, for $N = \{4, 5, 6, 7\}$. Integrals on the immersed boundary are approximated using 100×2^N evenly-spaced, evenly-weighted

quadrature points. The level of adaptive quadrature in the finite cell method used for volume integration is $l = 7$.[7] The results are shown in Figure A.13, indicating that the optimal convergence behavior of the formulation in Appendix A.1.4 can be retained on unfitted meshes, if sufficiently accurate quadrature is applied.
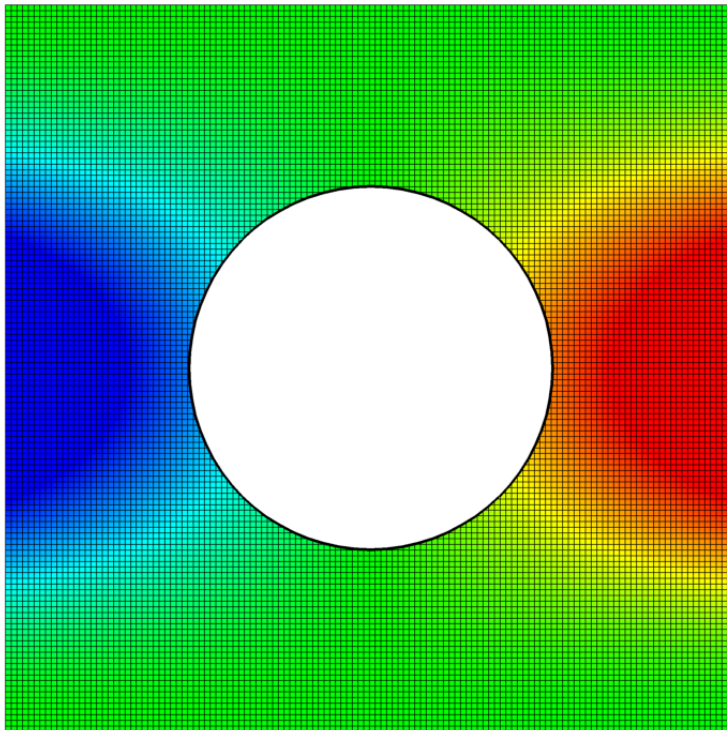

Figure A.12: Representative numerical solution to the poisson problem on the modified domain (A.42).

Remark 11. It is important to keep in mind the distinction between bulky immersed objects and immersed surfaces of co-dimension one to the domain. Although, in [7], we originally tried to develop thin-structure immersogeometric FSI formulations by degenerating finite cell discretizations, the finite cell discretization used in this section, with coarse Lagrange multipliers in the space proposed in Section 2.3, **does not** degenerate smoothly into the immersed surface formulation presented in the main body of the paper. The difficulty is illustrated in Figure A.14; flow entering the fluid domain through the portion of Γ_E on one side of the immersed structure would always be equal to flow exiting the other side, so the kinematic conservation property would be trivially (and pathologically) satisfied in spite of a net leakage. One might attempt to modify the definition of the space from Section 2.3 so that different constant multiplier values are permitted

---

[7]These choices of boundary and volume integration rules will eventually limit convergence rates, but are sufficient for optimal behavior at moderate resolutions. See [45] and [46, Section 4] for systematic numerical experiments on the influence of quadrature error in finite cell computations.
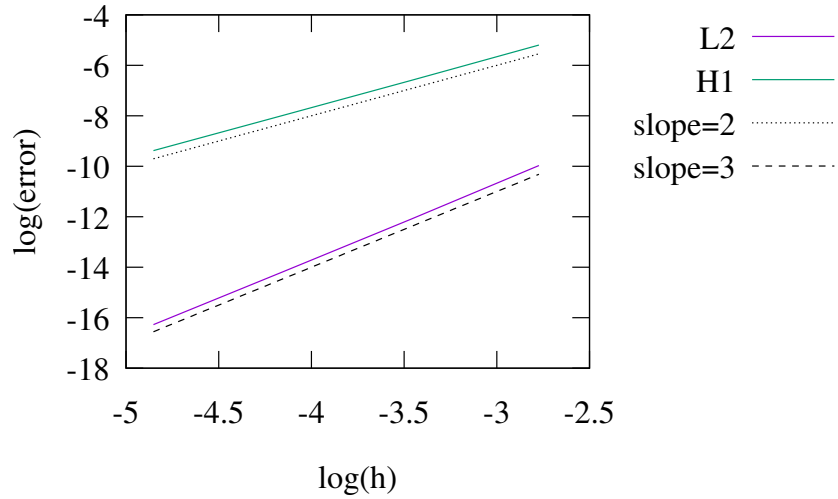
Figure A.13: Convergence of $L^2(\Omega)$ and $H^1(\Omega)$ errors using an unfitted mesh, showing optimal rates for $p = 2$.

on distinct simply-connected intersections of Γ with each block of 2^d Bézier elements, but then the stability becomes questionable. For intricate geometries of Γ, this could lead overconstraint and, for the degenerate case of a thin structure, there would be a nontrivial nullspace in the multiplier field, as only the difference of the multipliers from the two sides of the structure would be uniquely determined. The alternative "Lagrangian" definition of Λ^H depicted in Figure 3 of Section 2.3 would avoid the problem shown in Figure A.14, but also has questionable stability.
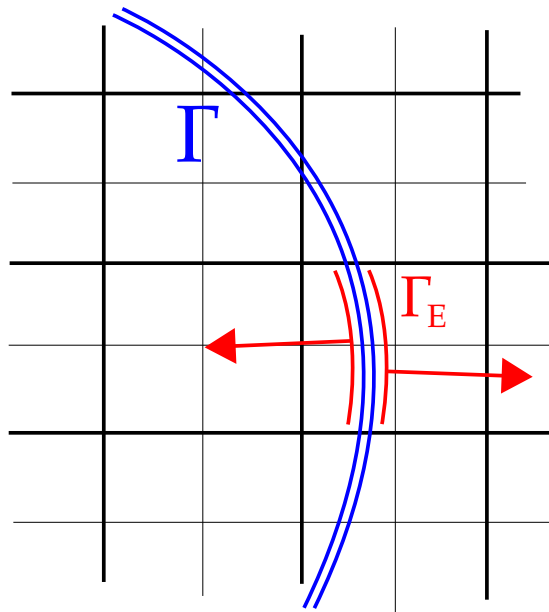

Figure A.14: For a nearly-degenerated structure, defining macroelements for Λ^H with the background grid in a naive way is ineffective for enforcing constraints on vector field components normal to an interface, because kinematic conservation will always be trivially satisfied.

References

[1] Y. Bazilevs, K. Takizawa, and T. E. Tezduyar. *Computational Fluid–Structure Interaction: Methods and Applications*. John Wiley & Sons, Chichester, 2013.

[2] Y. Bazilevs, M.-C. Hsu, and M. A. Scott. Isogeometric fluid–structure interaction analysis with emphasis on non-matching discretizations, and with application to wind turbines. *Computer Methods in Applied Mechanics and Engineering*, 249–252:28–41, 2012.

[3] I. Babuška. The finite element method with Lagrangian multipliers. *Numerische Mathematik*, 20:179–192, 1972.

[4] H. J. C. Barbosa and T. J. R. Hughes. The finite element method with Lagrange multipliers on the boundary: circumventing the Babuška-Brezzi condition. *Computer Methods in Applied Mechanics and Engineering*, 85(1):109–128, 1991.

[5] R. Stenberg. On some techniques for approximating boundary conditions in the finite element method. *Journal of Computational and Applied Mathematics*, 63(1):139–148, 1995.

[6] J. Nitsche. Über ein Variationsprinzip zur Lösung von Dirichlet-Problemen bei Verwendung von Teilräumen, die keinen Randbedingungen unterworfen sind. *Abhandlungen aus dem Mathematischen Seminar der Universität Hamburg*, 36:9–15, 1971.

[7] D. Kamensky, M.-C. Hsu, D. Schillinger, J. A. Evans, A. Aggarwal, Y. Bazilevs, M. S. Sacks, and T. J. R. Hughes. An immersogeometric variational framework for fluid–structure interaction: Application to bioprosthetic heart valves. *Computer Methods in Applied Mechanics and Engineering*, 284:1005–1053, 2015.

[8] M.-C. Hsu, D. Kamensky, Y. Bazilevs, M. S. Sacks, and T. J. R. Hughes. Fluid–structure interaction analysis of bioprosthetic heart valves: significance of arterial wall deformation. *Computational Mechanics*, 54:1055–1071, 2014.

[9] D. Kamensky, J. A. Evans, and M.-C. Hsu. Stability and conservation properties of collocated constraints in immersogeometric fluid-thin structure interaction analysis. *Communications in Computational Physics*, 18:1147–1180, 2015.

[10] M.-C. Hsu, D. Kamensky, F. Xu, J. Kiendl, C. Wang, M. C. H. Wu, J. Mineroff, A. Reali, Y. Bazilevs, and M. S. Sacks. Dynamic and fluid–structure interaction simulations of bioprosthetic heart valves using parametric design with T-splines and Fung-type material models. *Computational Mechanics*, 55:1211–1225, 2015.

[11] D. Kamensky, M.-C. Hsu, Y. Yu, J. A. Evans, M. S. Sacks, and T. J. R. Hughes. Immersogeometric cardiovascular fluid–structure interaction analysis using divergence-conforming B-splines. *Computer Methods in Applied Mechanics and Engineering*, 2016. http://dx.doi.org/10.1016/j.cma.2016.07.028.

[12] E. Burman. Projection stabilization of Lagrange multipliers for the imposition of constraints on interfaces and boundaries. *Numerical Methods for Partial Differential Equations*, 30(2): 567–592, 2014.

[13] M. Esmaily-Moghadam, Y. Bazilevs, T.-Y. Hsia, I. E. Vignon-Clementel, A. L. Marsden, and Modeling of Congenital Hearts Alliance (MOCHA). A comparison of outlet boundary treatments for prevention of backflow divergence with relevance to blood flow simulations. *Computational Mechanics*, 48:277–291, 2011.

[14] J. Kiendl, K.-U. Bletzinger, J. Linhard, and R. Wüchner. Isogeometric shell analysis with Kirchhoff–Love elements. *Computer Methods in Applied Mechanics and Engineering*, 198: 3902–3914, 2009.

[15] J. Kiendl. *Isogeometric Analysis and Shape Optimal Design of Shell Structures*. PhD thesis, Lehrstuhl für Statik, Technische Universität München, 2011.

[16] J. Kiendl, M.-C. Hsu, M. C. H. Wu, and A. Reali. Isogeometric Kirchhoff–Love shell formulations for general hyperelastic materials. *Computer Methods in Applied Mechanics and Engineering*, 291:280–303, 2015.

[17] D. Chapelle and K.-J. Bathe. The inf-sup test. *Computers & Structures*, 47:537–545, 1993.

[18] K.-J. Bathe. The inf–sup condition and its evaluation for mixed finite element methods. *Computers & Structures*, 79(2):243–252, 2001.

[19] A. Buffa, J. Rivas, G. Sangalli, and R. Vázquez. Isogeometric discrete differential forms in three dimensions. *SIAM Journal on Numerical Analysis*, 49(2):818–844, 2011.

[20] A. Buffa, G. Sangalli, and R. Vázquez. Isogeometric analysis in electromagnetics: B-splines approximation. *Computer Methods in Applied Mechanics and Engineering*, 199(17–20): 1143–1152, 2010.

[21] J. A. Evans and T. J. R. Hughes. Isogeometric divergence-conforming B-splines for the unsteady Navier–Stokes equations. *Journal of Computational Physics*, 241:141–167, 2013.

[22] J. A. Evans and T. J. R. Hughes. Isogeometric divergence-conforming B-splines for the unsteady Navier–Stokes equations. *Journal of Computational Physics*, 241:141–167, 2013.

[23] J. Pitkäranta. Local stability conditions for the Babuška method of Lagrange multipliers. *Mathematics of Computation*, 35(152):1113–1129, 1980.

[24] M. A. Puso, J. Sanders, R. Settgast, and B. Liu. An embedded mesh method in a multiple material ALE. *Computer Methods in Applied Mechanics and Engineering*, 245–246:273–289, 2012.

[25] M. R. Hestenes. Multiplier and gradient methods. *Journal of Optimization Theory and Applications*, 4(5):303–320, 1969.

[26] M. J. D. Powell. A method for nonlinear constraints in minimization problems. In R. Fletcher, editor, *Optimization*, pages 283–298. Academic Press, New York, 1969.

[27] C. Hesch, A. J. Gil, A. Arranz Carreño, and J. Bonet. On continuum immersed strategies for fluid–structure interaction. *Computer Methods in Applied Mechanics and Engineering*, 247-248:51–64, 2012.

[28] A.J. Gil, A. Arranz Carreño, J. Bonet, and O. Hassan. An enhanced immersed structural potential method for fluid–structure interaction. *Journal of Computational Physics*, 250: 178–205, 2013.

[29] T. Wick. Flapping and contact FSI computations with the fluid–solid interface-tracking/interface-capturing technique and mesh adaptivity. *Computational Mechanics*, 53 (1):29–43, 2014.

[30] C. Kadapa, W. G. Dettmer, and D. Perić. A fictitious domain/distributed Lagrange multiplier based fluid–structure interaction scheme with hierarchical B-spline grids. *Computer Methods in Applied Mechanics and Engineering*, 301:1–27, 2016.

[31] A. Campbell, T. Baldwin, G. Peterson, J. Bryant, and K. Ryder. Pitfalls and outcomes from accelerated wear testing of mechanical heart valves. *The Journal of Heart Valve Disease*, 5 Suppl 1:S124–132, 1996.

[32] S. Balay, S. Abhyankar, M. F. Adams, J. Brown, P. Brune, K. Buschelman, L. Dalcin, V. Eijkhout, W. D. Gropp, D. Kaushik, M. G. Knepley, L. C. McInnes, K. Rupp, B. F. Smith, S. Zampini, and H. Zhang. PETSc Web page. http://www.mcs.anl.gov/petsc, 2015.

[33] S. Balay, S. Abhyankar, M. F. Adams, J. Brown, P. Brune, K. Buschelman, L. Dalcin, V. Eijkhout, W. D. Gropp, D. Kaushik, M. G. Knepley, L. C. McInnes, K. Rupp, B. F. Smith, S. Zampini, and H. Zhang. PETSc users manual. Technical Report ANL-95/11 - Revision 3.6, Argonne National Laboratory, 2015.

[34] S. Balay, W. D. Gropp, L. C. McInnes, and B. F. Smith. Efficient management of parallelism in object oriented numerical software libraries. In E. Arge, A. M. Bruaset, and H. P. Langtangen, editors, *Modern Software Tools in Scientific Computing*, pages 163–202. Birkhäuser Press, 1997.

[35] MUMPS: a MUltifrontal Massively Parallel sparse direct Solver. http://mumps.enseeiht.fr/. Accessed 24 April 2016.

[36] V. Hernandez, J. E. Roman, and V. Vidal. SLEPc: A scalable and flexible toolkit for the solution of eigenvalue problems. *ACM Trans. Math. Software*, 31(3):351–362, 2005.

[37] V. Hernandez, J. E. Roman, and V. Vidal. SLEPc: Scalable Library for Eigenvalue Problem Computations. *Lect. Notes Comput. Sci.*, 2565:377–391, 2003.

[38] J. E. Roman, C. Campos, E. Romero, and A. Tomas. SLEPc users manual. Technical Report DSIC-II/24/02 - Revision 3.7, D. Sistemes Informàtics i Computació, Universitat Politècnica de València, 2016.

[39] C. L. Chang and John J. Nelson. Least-squares finite element method for the Stokes problem with zero residual of mass conservation. *SIAM Journal on Numerical Analysis*, 34(2):480–489, 1997.

[40] J. A. Evans, T. J. R. Hughes, and G. Sangalli. Enforcement of constraints and maximum principles in the variational multiscale method. *Computer Methods in Applied Mechanics and Engineering*, 199(1–4):61–76, 2009.

[41] T. Ellis, L. Demkowicz, and J. Chan. Locally conservative discontinuous Petrov–Galerkin finite elements for fluid problems. *Computers & Mathematics with Applications*, 68(11): 1530–1549, 2014.

[42] L. Demkowicz. Babuška $\Longleftrightarrow$ Brezzi? Technical Report 06-08, ICES, UT Austin, 2006.

[43] E. H. van Brummelen, K. G. van der Zee, V. V. Garg, and S. Prudhomme. Flux evaluation in primal and dual boundary-coupled problems. *Journal of Applied Mechanics*, 79:010904, 2011.

[44] D. Schillinger and M. Ruess. The Finite Cell Method: A review in the context of higher-order structural analysis of CAD and image-based geometric models. *Archives of Computational Methods in Engineering*, 22(3):391–455, 2015.

[45] A. Stavrev. *The Role of Higher-Order Geometry Approximation and Accurate Quadrature in NURBS Based Immersed Boundary Methods*. Master's thesis, Technische Universität München, Munich, Germany, 2012.

[46] D. Schillinger, I. Harari, M.-C. Hsu, D. Kamensky, S.K.F Stoter, Y. Yu, and Y. Zhao. The non-symmetric Nitsche method for the parameter-free imposition of weak boundary and coupling conditions in immersed finite elements. *Computer Methods in Applied Mechanics and Engineering*, 309:625–652, 2016.